Microstructure, interfaces and properties of 3YTZP ceramic composites with 10 and 20 vol% different graphene-based nanostructures as fillers.

Carmen Muñoz-Ferreiro [a], Ana Morales-Rodríguez [a], Teresa Cristina Rojas [b], Emilio Jiménez-Piqué [c,d], Cristina López-Pernía [a], Rosalía Poyato [b], Angela Gallardo-López [a,*]

[a] Dpto. de Física de la Materia Condensada, ICMS, CSIC- Universidad de Sevilla, apdo. 1065, 41080 Sevilla, Spain

[b] Instituto de Ciencia de Materiales de Sevilla, ICMS, CSIC-Universidad de Sevilla, Avda. Américo Vespucio 49, 41092 Sevilla, Spain

[c] Dpto. de Ciencia de los Materiales e Ingeniería Metalúrgica, Universidad Politécnica de Cataluña, Avda. Eduard Maristany 10-14, 08019 Barcelona, Spain

[d] Barcelona Research Center in Multiscale Science and Engineering, Universidad Politécnica de Cataluña, Avda. Eduard Maristany 10-14, 08019 Barcelona, Spain

*Corresponding author. E-mail address: angela@us.es

Phone numbers: +34 620612167, +34 954554448

Abstract

The graphene family comprises not only single layer graphene but also graphene-based nanomaterials (GBN), with remarkably different number of layers, lateral dimension and price. In this work, two of these GBN, namely graphene nanoplatelets (GNP) with n~7-15 layers and few-layer graphene (FLG) with n~3 layers have been evaluated as fillers in 3 mol% yttria stabilized tetragonal zirconia (3YTZP) ceramic composites. Composites with 10 and 20 vol% GNP or FLG have been fabricated by wet powder processing and spark plasma sintering (SPS) and the influence of the content and number of layers of the graphene-based filler has been assessed. For both graphene-based fillers, an intermediate zirconia oxycarbide has been detected in the grain boundaries. The lower stacking degree and much more homogeneous distribution of the FLG, revealed by transmission electron microscopy (TEM), can improve load transfer between the GNPs and the ceramic matrix. However, high FLG contents lower densification of the composites, due partly to the larger FLG interplanar spacing also estimated by TEM. The hardness (both Vickers and nanoindentation) and the elastic modulus decrease with increased GBN content and with improved graphene dispersion. The FLG greatly inhibit the crack propagation that occur perpendicular to their preferential orientation plane. The composites with thinner FLG have higher electrical conductivity than those with GNP. The highest electrical conductivity is achieved by composites with 20 vol% FLG in the direction perpendicular to the compression axis during sintering, $\sigma_{\perp}$= 3400 ± 500 Sm^{-1}.

Keywords: ceramics, composite materials, nanostructures, grain boundaries, transmission electron microscopy: TEM, electrical conductivity.

1. Introduction

The reasons for using graphene-based nanostructures as fillers for ceramic composites are multifold. From the mechanical point of view, the intrinsic fragility of ceramics could be overcome by a nanostructured material which possesses an extremely high elastic modulus (1 TPa) [1] and offers microscopic reinforcement mechanisms as crack deflection, grain wrapping and crack bridging. An interesting fracture toughness improvement has been reported in Si_3N_4 composites with GNP [2,3]. From the thermal

point of view, the high thermal conductivity of graphene can improve the response of ceramics to thermal shock [4]. From the electrical point of view, the ballistic electron transport properties exhibited by graphene monolayers can also improve the conductivity in ceramic composites containing graphene, and these electro-conductive ceramics could be machined in complex shapes thanks to the electro discharge machining technique (EDM) [5]. In view of these interesting properties, the study of graphene ceramic composites is rising at a constant pace, and the carbon nanostructures used previously as fillers such as carbon nanotubes are being extensively replaced by the use of graphene-based nanomaterials (GBN). However, under the general denomination of GBN, the stacking of a variable number of graphene layers ranging from 3 to 150 is included, while multilayer graphene (MLG) refers only to $n \leq 10$ layers. These graphene-based nanostructures differ in many aspects. The most obvious is size, not only because of the different thickness related to the number of layers but also because they often have different lateral dimensions as well. Their electronic structure also depends on the number of layers [6]. While the electronic band structure of monolayer graphene consists of linear bands without a gap between the valence and conduction bands, bilayer graphene possesses parabolic bands and a gap may be induced by an electric field. The electronic structure complicates as the number of layers increases until it stabilizes for $n \geq 10$ which corresponds to the graphite electronic structure. The interplanar spacing is also influenced by the number and the ordering of the stacking layers. While the interplanar spacing for graphite is 3.32 Å, it increases to 3.42 Å for disordered or turbostratic graphite, and approaches the 3.4 Å spacing for bilayer graphene. Although some procedures for obtaining GBN from graphite are rather simple, the economic cost of the graphene-based nanostructures when the number of layers diminishes rises considerably. Therefore, the fabrication cost of graphene-based nanostructures varies in a wide range.

In spite of these differences, a main common feature to the graphene-based structures should be highlighted: their high specific surface area. This feature, together with the relevance of “graphene” in the media, is the reason why graphitic nanostructures consisting of the stacking of more than 10 graphene layers, which could be strictly considered as graphite are actually commercialized and known by the denomination “graphene platelets” or “graphene nanoplatelets”, the latter when thickness is < 100 nm.

These noticeable differences in size, number of layers and cost between the so called graphene-based nanomaterials raise the interest to evaluate their distinct performance in ceramic composites. Key issues which are not completely solved in the development of the ceramic composites with graphene-based reinforcements, such as the homogeneous dispersion of the graphene-based nanostructures in the ceramic matrix, the full densification of the composites and the interfacial structure between the GBN and the ceramic matrix, are certainly influenced by the type of two-dimensional GBN used. Besides, these issues increase in complexity when the GBN content in the composites increases.

While some of these key issues are being treated in depth in particular ceramic composites, such as alumina or silicon nitride [3,7], other ceramic matrices still need systematic studies to account for these microstructural features and for improvements in their properties when incorporating GBN. This is the case of 3YTZP, a biocompatible ceramic characterized by its high toughness and which presents ionic conductivity at high temperature. Properties as the fracture toughness or the electrical conductivity can be enhanced with the addition of GBN to this 3YTZP ceramic [8,9]. In particular, the study of the influence of the number of stacking layers of graphene-based nanostructures on the properties of these ceramic composites has not been assessed yet, and an investigation of the interfaces in GBN/3YTZP composites needs to be carried out to understand the reinforcing mechanisms.

In this work, the influence of the number of stacking layers of graphene-based nanostructures on the microstructural homogeneity, densification, interfacial structure, hardness, elastic modulus and crack propagation of ceramic composites with a 3YTZP matrix are analyzed. For this purpose, the fabrication of 3YTZP composites with two radically different graphene-based nanostructures has been addressed, and the effect of adding substantially different graphene-based nanostructure contents (10 and 20 vol%) has also been evaluated. These high filler contents are used in order to obtain a high electrical conductivity in the composites.

2. Experimental

Commercial 3YTZP powders with 40 nm particle size were acquired from Tosoh Corporation (Tokyo, Japan) and annealed in air at 850°C for 30 min to enhance sintering. The two graphene-based nanomaterials were supplied by Angstrong Materials

(Dayton, Ohio, USA), with the following specifications: (i) graphene nano platelets (GNP) with 20-40 nm thickness and ≤ 5 μm planar diameter and (ii) few-layer graphene (FLG) with n≤ 3 graphene layers and ≤ 10 μm planar diameter. Both GBNs were dispersed in isopropanol, subjected to probe ultrasonication and mixed with the ceramic powder as described elsewhere [10]. Mixtures containing 3YTZP with 10 and 20 vol% GNP or FLG nominal content were prepared. The composites with GNP will be named hereafter Z10G and Z20G while Z10F and Z20F will stand for the composites with FLG.

The composite powders were subjected to elemental analysis to check for the real C content (equivalent to the real GBN content in this case) of the composites to evaluate deviations from the nominal content that could take place during processing. Three measurements were carried out for each batch with a TruSpec CHNS micro LECO.

Sintering of the composite powders was carried out in a SPS furnace model 515 S, Dr. Sinter Inc. at 1250°C, with a sintering time of 5 min, heating and cooling ramps of 300°C and 50°C per minute, respectively, and a uniaxial pressure of 75 MPa, as described in [10]. The cylindrical pellets of 15 mm diameter and ~3 mm height were manually grinded, cut at low-speed and polished when necessary up to a 1 μm final size.

The influence of the GBN content and number of layers on the crystallographic phases of the 3YTZP matrix was evaluated by X-ray diffraction (XRD) on the sintered composites. A X-ray D8 Advance A2, (Bruker Co.) diffractometer with θ:θ configuration and a Bragg-Brentano geometry was used. XRD was also performed on the as-received GNP.

The density of the sintered composites was measured by the Archimedes method using a precision scale and distilled water as immersion medium. The theoretical density was calculated by the rule of mixtures using the experimental volume fraction of the corresponding GBN (from elemental microanalysis). To evaluate the integrity of the graphene-based nanostructures after the sintering process, Raman spectroscopy was carried out on the composite fracture surfaces with a dispersive microscope Raman

Horiba Jobin Yvon LabRam HR800, with a green laser He-Ne (532.1 nm). Seven to ten spectra were taken from each composite.

To account for the degree of dispersion of the GBN in the zirconia matrix, as well as to account for any structural anisotropy of the composites, polished in-plane and cross-section surfaces were analysed by conventional scanning electron microscopy (SEM) using backscattered electrons for imaging, with a JEOL 6460LV microscope. Polished cross sections annealed in air for 15 min at 1150ºC were also examined by high resolution scanning electron microscopy (HRSEM) to estimate the influence of the number of layers and content of the GBN on the grain size of the 3YTZP ceramic matrix. The value of the planar diameter, *d*, namely the diameter corresponding to a circle with the same area as the measured grain, was chosen for the grain size, averaging 200-300 grains from each composite. The fracture surfaces of the composites were also examined by HRSEM to observe the graphene-based nanostructures (GNP or FLG) incorporated to the ceramic matrix.

Transmission electron microscopy (TEM) characterization was also performed in the composites with 10 vol% GNP or FLG in order to analyse the ceramic-GBN interfaces and to assess the GBN stacking. For this purpose, thin foils from cross-section surfaces were prepared following the conventional procedure of mechanical polishing followed by argon ion milling to electron transparency. A FEI Tecnai field emission gun scanning transmission electron microscope (STEM-FEG), mod. G2F30 with an S-Twin objective lent, operated at 300 kV, with 0.2 nm point resolution, and equipped with a high angle annular dark field (HAADF) detector from Fischione with 0.16 nm resolution in STEM-HAADF mode, was used. A Gatan Imaging Filter (GIF) attached to the Tecnai microscope (QUAMTUM SE model) was used for electron energy-loss spectroscopy (EELS) studies. The EELS spectra were recorded in STEM mode using a probe with a size of less than 1 nm, with a spectrometer collection angle of 9.6 mrad. Under these conditions, the energy resolution of the couple microscope/spectrometer system was ~0.8 eV.

The composites hardness was estimated on in-plane and cross sections from at least 10 Vickers indentations performed with a Vickers Duramin 5 microindenter (Struers) with loads of 1.96 N. Higher loads (up to 30 kN) were also applied with a Wilson indenter to

create fractures from the corner of the imprints, which have been observed by optical microscopy to assess crack propagation. However, since the Vickers hardness from residual imprints does not take into account the elastic relaxation upon unloading, which is particularly important in ceramics, nanoindentation tests which measure hardness at a maximum load were performed. A MTS Nanoindenter XP with a fully calibrated Berkovich tip and a continuous stiffness measurement module, as described in [11] was used. The hardness (H) and Young's modulus (E) were calculated as a function of penetration depth using the method proposed by Oliver and Pharr [12].

The electrical conductivity of the sintered composites was estimated in a two-point configuration at room temperature in the directions parallel and perpendicular to the compression axis during SPS ($\sigma_{//}$, $\sigma_{\perp}$). The specimens were cut into parallelepipeds and the electrodes were two parallel faces coated with colloidal silver varnish. Two different equipments were used to validate the results of the impedance spectroscopy measured: an Agilent 4294A analyzer in the 100 Hz - 2 MHz frequency range and a Solartron SI 1260A (CITIUS-Sevilla), which used a potentio-dynamic method with a 0-10 mV range in steps of 1mV. The measurements were validated also in AC, with a frequency sweep from 100 to 1000 Hz at 10 mV. With the potentio-dynamic method, several measurements were taken in each configuration. For each measurement, the electrodes were removed with acetone and new colloidal silver painting was applied.

3. Results and discussion

3.1. Microstructural characterization of the composites

The real volume fraction of the graphene-based fillers in the composites powder is very similar to the nominal content of GNP or FLG, but there are small discrepancies that arise during processing, due to losses of the GBN (in the composites Z10G and Z10F) or losses of the ceramic powder (in the composites Z20G and Z20F) as indicated in table 1. These discrepancies are completely random and not significant.

Table 1. Data corresponding to the 3YTZP composites sintered in this study indicating the type of graphene-based filler (graphene nanoplatelets (GNP) or few-layer graphene (FLG)), nominal and experimental content, density and grain size.

		GBN content		Density		Grain size
Sample	**GBN Filler**	**Nominal** (vol %)	**Exp.** (vol%)	ρ_{exp} (g/cm^3)	ρ_{rel} (%)	d_{planar} (μm)
3YTZP[10]	_	0	0	6.1	100	0.29 ± 0.02
Z10G	GNP	10	9.0	5.6	99	0.22 ± 0.10
Z20G	GNP	20	23.4	5.2	100	0.14 ± 0.06
Z10F	FLG	10	8.7	5.5	98	0.14 ± 0.06
Z20F	FLG	20	21.4	4.8	95	0.18 ± 0.09

The composites with GNP are fully dense, near 100% theoretical density, while the density of the composites with FLG is slightly lower (≥ 95%) and decreases with increasing FLG content, as indicated in table 1. Since the composites with FLG do not show porosity in the ceramic matrix (see fig. s1 in the supplementary data), the decrease in density must be associated to the FLG small number of layers and high specific surface, since there are many individual FLG for a given GBN content. These composites are very hydrophilic and absorb water on their surface during immersion [13], thus requiring longer stabilization times for the measurements.

All the sintered composites, regardless of the type and content of graphene-based filler (GNP or FLG) present the reduced tetragonal zirconia phase as the main crystallographic phase ($ZrO_{1.95,}$ JCPDS 01-081-1544), as it can be seen in figures 1a and 1b. The reduction of the zirconia takes place during SPS, due to the highly reducing atmosphere of the graphite mould containing the powders and the absence of oxygen (vacuum). The XRD patterns from the composites with GNP (fig. 1a) present the main graphite peak (2θ= 26.6º) (JCPDS 00-026-1076), in agreement with the results from composites with smaller GNP contents [10]. This peak is not a consequence of the degradation of the GNP, but it rather reflects the crystal structure of this nanomaterial with a stacking of 100-150 graphene layers. The XRD performed to the as-received GNP powders (not shown) indicates that they are highly ordered graphite stacks, with only a sharp reflection at (002) and a small one at (004). The X-ray diffractograms of the composites with FLG (fig. 1b) only show the reduced $ZrO_{1.95}$ tetragonal zirconia phase and not the main graphite peak, as expected since this graphene-based nanostructure has less than 10 layers according to the supplier (n≤3 layers).

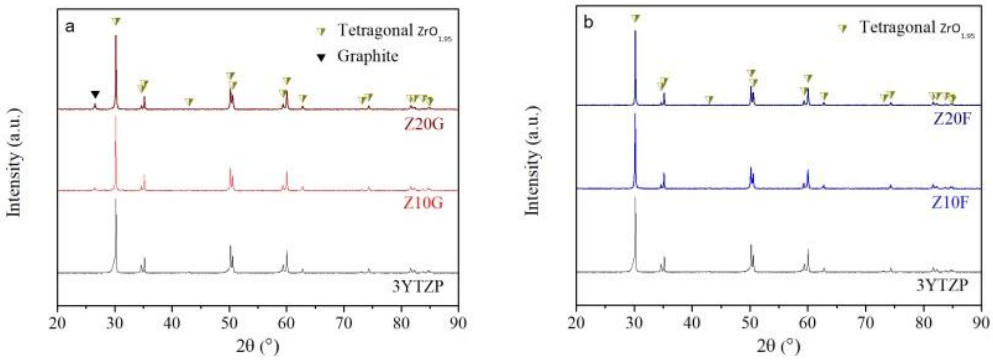

Figure 1. X-ray diffractograms for the 3YTZP composites with (a) GNP and (b) FLG. The peaks corresponding to the reduced tetragonal $ZrO_{1.95}$ and graphite are indicated. XRD of monolithic 3YTZP from the same powder and same sintering conditions has been added for comparison.

The Raman spectra acquired on the fracture surfaces of the different composites sintered in this study exhibit the same bands as the as-received graphene-based filler (fig. 2a and b), included for comparison, indicating that none of the graphene-based nanostructures have been damaged during sintering. All the spectra show the characteristic D, G and 2D bands corresponding to GBNs at ~1350, ~1580 and ~2700 cm^{-1} [14], respectively. They have been normalized to the G band for easier comparison. The D band is frequently associated to crystallographic defects in the graphitic structures, but it is also related to the crystallite size [15]. Some authors have proven that the D band in the Raman spectrum taken at the centre of a graphene nanoplatelet is non-existent, while it develops and increases at the borders of the GNP layer [16]. The most relevant difference in the Raman spectra of the two GBNs used and their corresponding composites are the I_D/I_G ratio and the 2D band intensity. The FLG has much higher I_D/I_G values (1.10) than the GNPs (0.13) because of their larger specific surface and the same happens for their composites. Besides, for a certain volume of GBN there will be a higher number of graphene borders for the FLG (larger number of individual FLG) than for the GNPs (smaller number of individual GNPs and consequently fewer borders). The larger number of individual FLG also contributes to a higher disorder. This is not completely unexpected since the borders of any crystal structure are just defects or deviations of the ideal infinite crystal structure. Therefore, while an increase of the I_D/I_G

ratio of the graphitic phase usually corresponds to a more defective crystal structure, it can also account for a smaller size, as it is the case for the FLG. Another difference between the Raman spectra is a shift difference of ~8 cm^{-1} to higher frequency values for the G band position of the FLG with respect to that of the GNPs. This shift indicates a smaller number of graphene layers in the FLG [17].

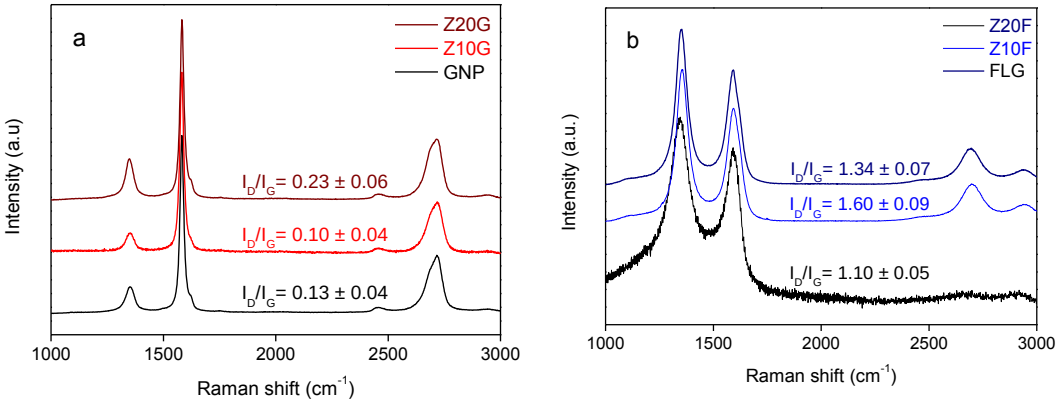

Figure 2. Raman spectra of the 3YTZP composites with 10 and 20 vol% (a) GNP and (b) FLG compared to the spectra of the as-received GNP and FLG respectively. The experimental I_D/I_G ratios are indicated.*From Ref.[10] . **From Ref. [39].

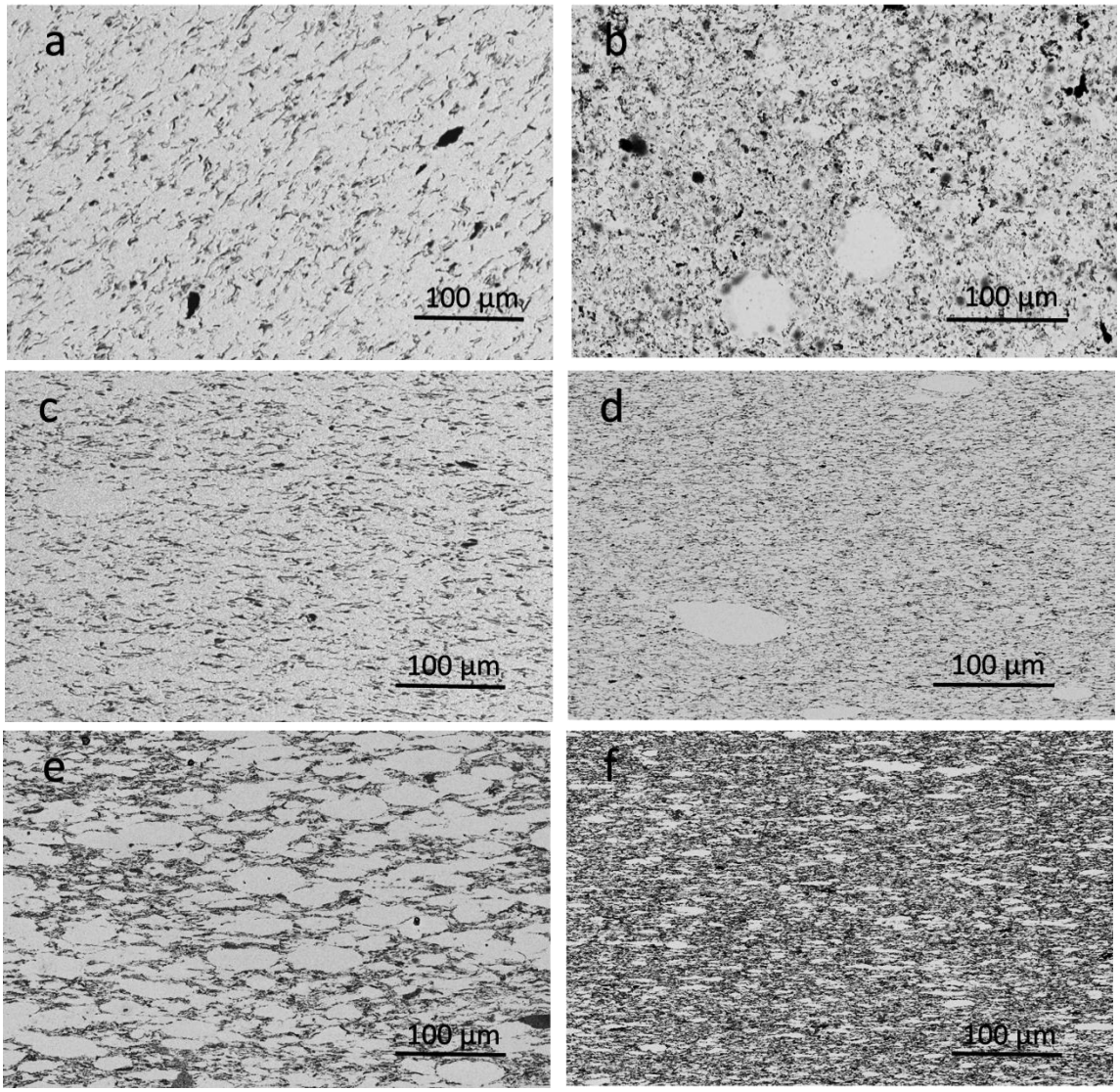

Figure 3. SEM micrographs with BSE contrast of (a, b) in-plane and (c, d, e, f) cross section polished surfaces of the 3YTZP composites with (a, c) 10 vol% GNP, (b, d) 10 vol% FLG, (e) 20 vol% GNP and (f) 20 vol% FLG where the light phase corresponds to the 3YTZP ceramic and the dark phase to the GBN.

The backscattered electrons SEM micrographs of polished surfaces shown in figure 3 serve to assess the homogeneity in the distribution of the GNP or FLG in the ceramic matrix. The light phase observed in the micrographs corresponds to the zirconia matrix while the dark phase corresponds to the graphene-based nanostructure (GNP/FLG). The cross sections (parallel to the sintering axis) of all composites show a preferential orientation of the graphene nanostructures. Since the major surface (ab plane) of the graphene layers lies in a plane perpendicular to the SPS sintering axis, the cross sections show a side view of the graphene-based structure, where a clear alignment of the

nanostructures can be detected. Conversely, on the in-plane surface, the GBN orientation is somehow random, as expected, although platelet-like forms are not abundant. This is due to the fact that these graphene-based fillers wrap the ceramic grains, thus adopting tortuous shapes. The high structural anisotropy of the ceramic composites is due to the intrinsic two dimensional character of the GNB, together with their preferential alignment with the uniaxial sintering pressure, and it affects significantly the macroscopic properties of these materials, as it has been pointed out in the literature [18–20]. The composites with GNP present rather uniformly distributed graphene Nanoplatelets with some interconnected and/or stacked GNP (arrowed in figure 3a and b), and some clean ceramic areas. These ceramic areas are approximately circular in the in-plane surfaces of the composites and oval in the cross sections, with an estimated major axis of 30-100 μm and evidence that the GNP did not mix completely with the 3YTZP ceramic powder during the processing. The FLG, due to its smaller size, can be better dispersed in the ceramic powder and it has been found much more homogeneously distributed in the sintered composites than the GNP for the same GBN content using the same processing routine. This homogenization routine has proven quite successful for lower GNP content (1 and 5 vol%) in the same 3YTZP matrix, although some agglomeration occurred. The homogenization routine for high GNP content can be enhanced using higher energy mechanical agitation like planetary ball milling, as it has been proven recently for 3YTZP with 10 vol% GNP [21].
The composites with FLG also present clean ceramic areas, although in a lesser extent than those with GNP, with an estimated major axis of 5-100 μm and 3-30 μm for Z10F and Z20F, respectively.

The fracture surfaces of the sintered composites observed by HRSEM show the characteristic shapes of the graphene-based nanostructures embedded in the ceramic matrix (figure 4). The dimensions of the isolated GNPs found among the ceramic grains have been estimated (d_{planar} < 5 μm and thickness ~20 nm) though the GNP are most commonly found stacked or interconnected forming small groups (fig. 4b) as it was already pointed out from low magnification BSE observations (fig. 3). These interconnected groups have sizes (d~10 μm) much larger than the 3YTZP ceramic grain size, so when the magnification of the micrographs is set to see one of the phases (either GNP or 3YTZP), the other one cannot be observed properly. GNP pull outs can be observed protruding from the ceramic surface like rigid structures, as fine flat flakes,

due to the high number of graphene layers of these structures. Pull outs are a toughening mechanism which has been observed in composites with different matrices [22]. GNPs show flat and wavy surfaces (fig 4a and b), as well as wrinkles and folding (fig. 4a) of the borders of the Nanoplatelets.

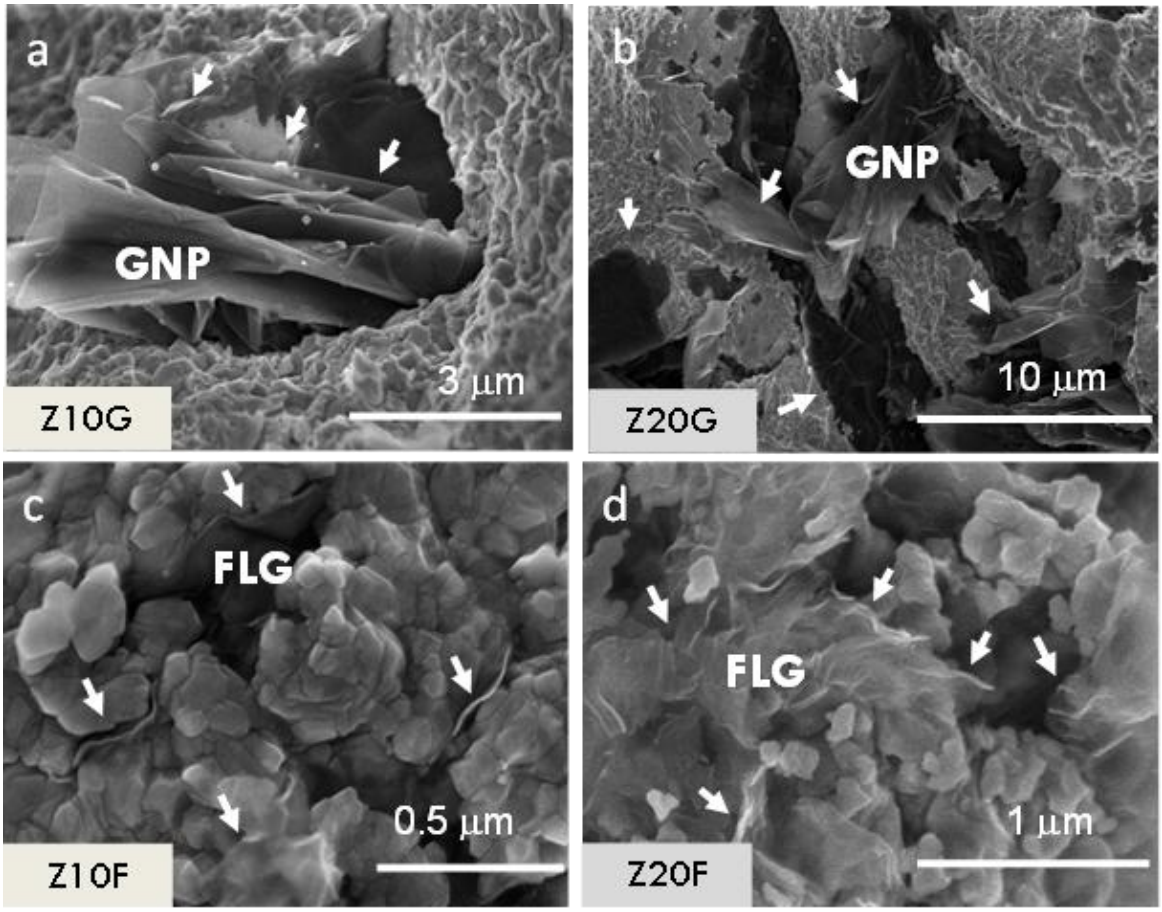

Figure 4. SEM micrographs of the fracture surfaces of the 3YTZP composites with (a) 10 vol% GNP, (b) 10 vol% FLG, (c) 20 vol% GNP and (d) 20 vol% FLG. GNPs and FLG are arrowed.

The morphology of the FLG in the fracture surface of the 3YTZP/FLG sintered composites (Figure 4 c and d) is radically different from that of the GNP. The few layer graphene is perceived as a fine, wavy, semi-transparent tissue covering the ceramic grains, similar to what has been reported in alumina composites [23] and show corrugated surfaces. Their size is smaller (d_{planar} < 10 μm), not too different from the 3YTZP ceramic grain size. The large difference in the number of layers between GNP and FLG can be clearly inferred from the size, shape and appearance of both phases in

the composites. Side views of the FLG (with estimated thickness < 3 nm) have been indicated in figures 4 c and d. The graphene-based sheets are well dispersed in the ceramic matrix, some of them are isolated but most of them are stacked in small groups and/or forming interconnected networks (fig. 4d).

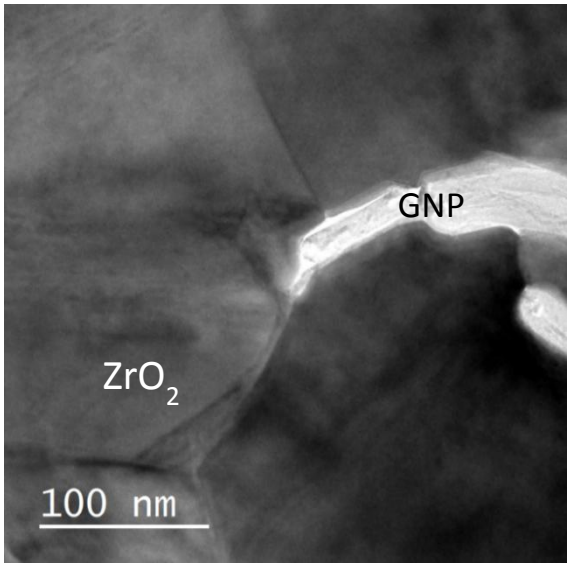

Figure 5. TEM general image of the composite Z10G.

The GNP rigidity inferred from the SEM observations seems to be due to the GNP stacking, since high magnification TEM examination reveals the flexible nature of the isolated GNP and their accumulation at the 3YTZP grain boundaries, thus allowing them to bend and re-adjust with conformity, as illustrated in figure 5. The general TEM image in figure 5a shows the GNPs (bright contrast) dispersed in the 3YTZP matrix. The GNP occupy quite large regions, 4-5 µm lateral size and ~0.2-1 µm thick. The latter indicates the stacking of multiple GNPs. The high GNP surface roughness could enhance the chemical reactivity by improving the interfacial bonding with the matrix. Between the GNP regions and the 3YTZP grains, three different types of interfaces have been detected by high resolution electron microscopy (HREM) and EELS: (i) abrupt and crystalline with a firm connection and lattice fringes of 3.4 Å and 2.6 Å, corresponding to planes of both phases (figure 6a). (ii) Crystalline interfaces with d-spacing not coincident with GNP nor ZrO_2 (figure 6b), and (iii) amorphous regions of ~5 nm thickness (Figure 6c). In figure 7, the EELS spectra, C-K, O-K and Zr-$M_{2,3}$ edges, measured on the ceramic matrix (point 1), on a GNP region (point 2) and on the interface (point 3) are depicted. The presence of C, Z, and O elements in this last point, indicates the formation of an intermediate zirconia oxycarbide phase via a chemical reaction that occurs in the interface [24].

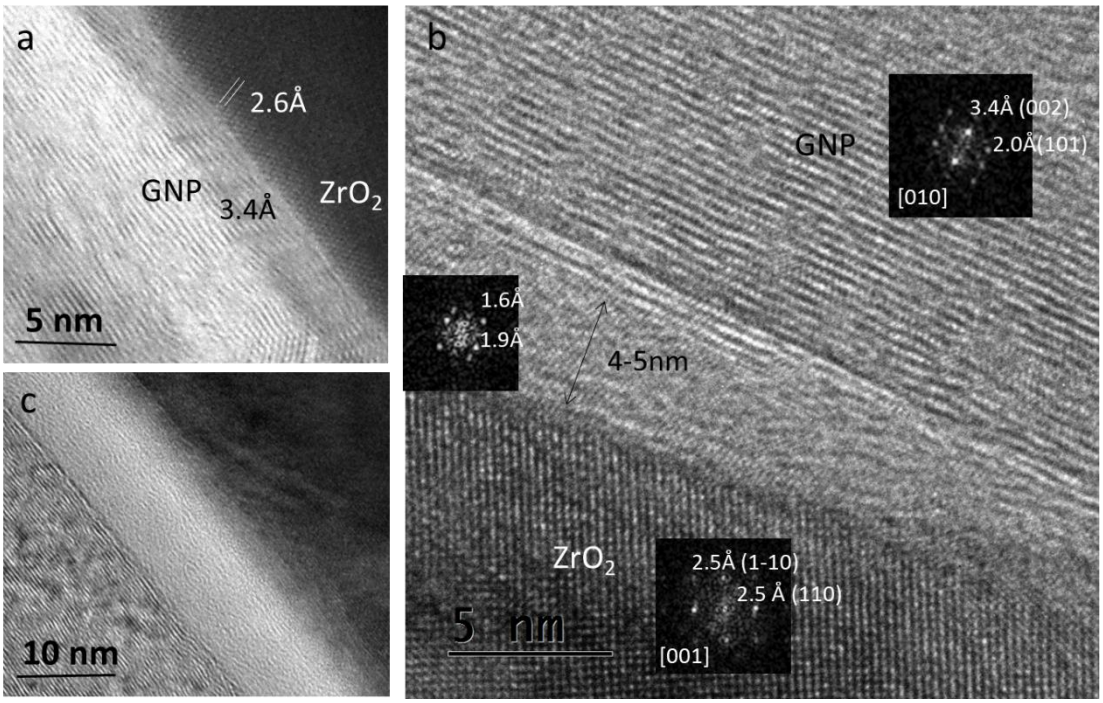

Figure 6. HRTEM images of different 3YTZP/GNP interfaces observed in the composite Z10G.

The general HAADF-STEM or Z-contrast image of figure 8a shows that the FLG is well dispersed in the zirconia matrix, and reveals its curved and flexible nature. The composite with FLG presents a more uniform distribution of the graphene-based nanostructure into the ceramic matrix than the composite with GNP. However, in some areas, accumulation of FLG (~50 nm thick) is observed (darker regions). The FLGs are interconnected through the 3YTZP grain boundaries, forming 2-5 nm thick regions (figure 8), indicating that the individual FLG are either isolated or stacked with a maximum number of 5 nanosheets. D-spacings in the range of 3.6 to 4 Å have been measured (a distance of 3.7 Å is indicated in figure 8b), which are higher values than the theoretical distance (3.32 Å) between two layers of the graphene phase hexagonal structure (i.e. (002) spacing) in graphite. This can be explained by a weakening of the π–electron stacking attraction between the graphene layers due to the 3YTZP grains as previously reported for Al_2O_3 nanoparticles [24]. The weakening of the π-electron stacking attraction is also observed in bilayer graphene with respect to graphite (3.4 Å d-spacing), and can contribute to the lower density of the composites with FLG, although this effect probably plays a very minor role. Amorphous regions of ~5-20 nm thickness are also observed between the ceramic crystalline grains. The EELS spectra measured on the interfaces of Z10F composite (figure 9) show the presence of C, Zr and

O elements indicating -as in the composite with GNP- that a chemical reaction has led to the formation of an intermediate zirconia oxycarbide amorphous phase. This kind of 3YTZP/FLG interface phase, also present in Z10G composite, can enable efficient load transfer, thus delaying failure through impediment of crack propagation.

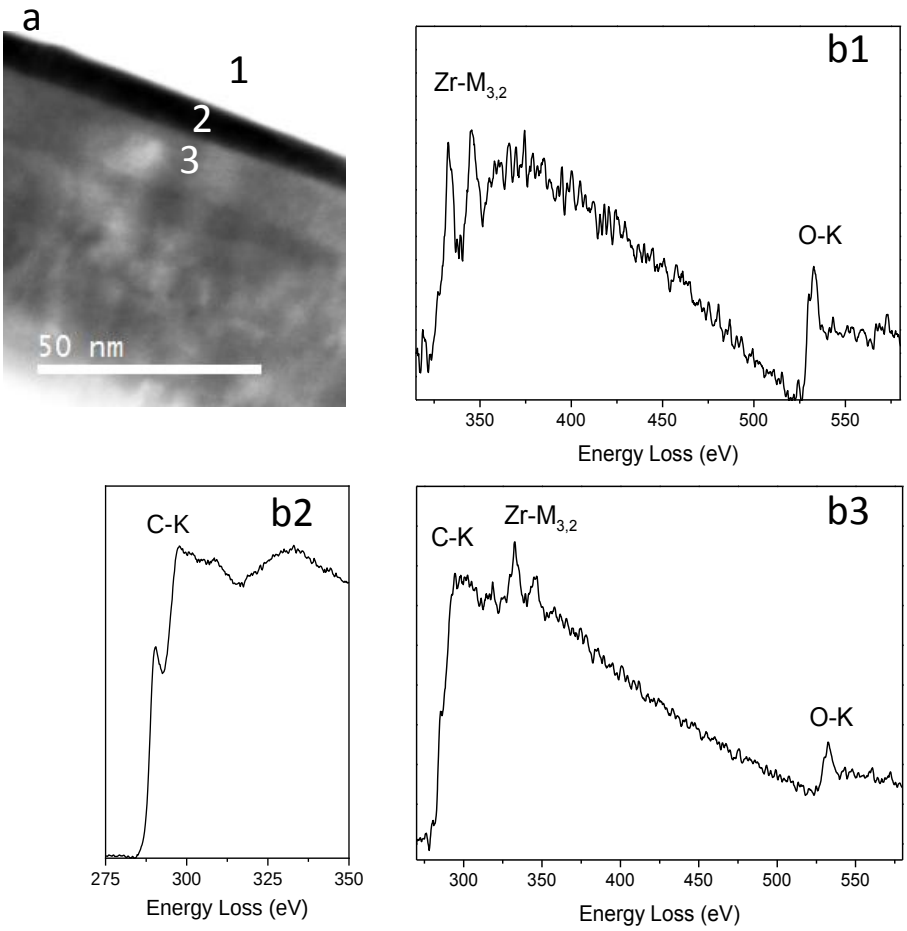

Figure 7. (a) HAADF-STEM or Z-contrast image of Z10G composite and (b) EELS spectra (C-K, O-K and Zr-$M_{2,3}$ edges) measurements in points (1) 3YTZP ceramic grain, (2) GNP region and (3) interface marked in (a).

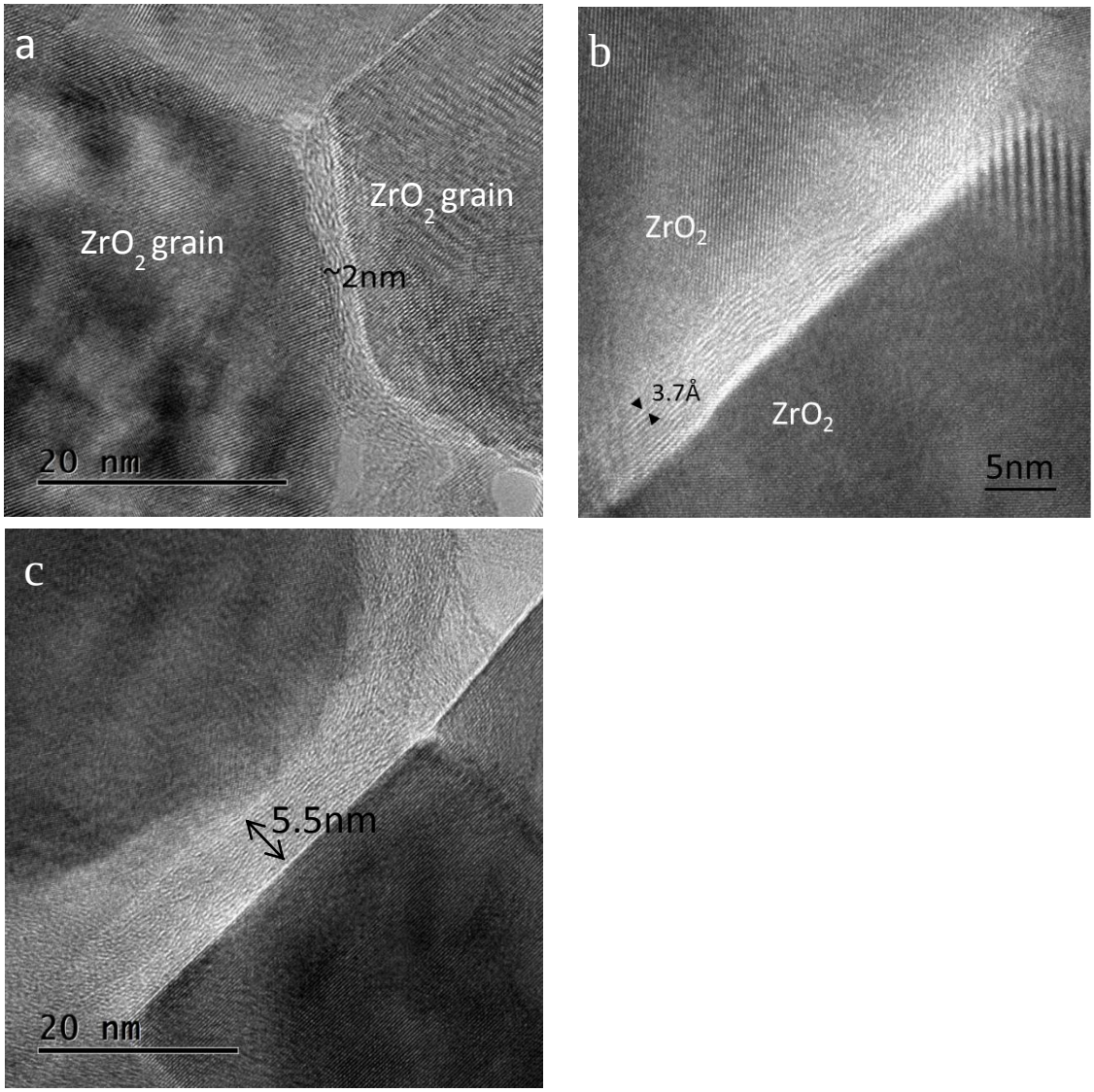

Figure 8. HRTEM images of 3YTZP / FLG interfaces in the composite Z10F.

The values of the ceramic grain size for the different composites, and for the monolithic 3YTZP ceramic prepared with the same sintering conditions for comparison, are detailed in table 1. The ceramic grains are equiaxed independently of the amount and number of layers of the GBN incorporated to the composite, with an estimated shape factor F = 0.73 ± 0.08, analogous to the monolithic 3YTZP ceramic. The introduction of a graphene-based phase has a slight refinement effect on the zirconia grain size in the composites, in accordance to what has been reported in the literature [25]. The grain size of the composites with GNP decreases with increasing GNP content from 10 to 20 vol%, while the increase of the FLG content does not reduce the grain size any more in the corresponding composites.

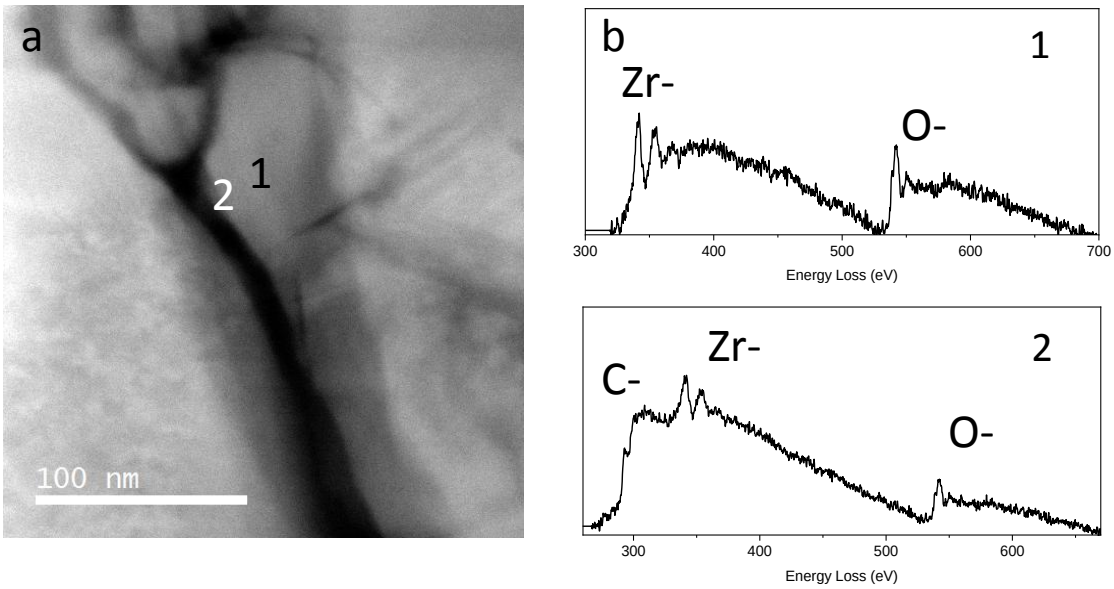

Figure 9. HAADF-STEM or Z-contrast image of the Z10F composite and (b) EELS spectra (C-K, O-K and Zr-$M_{2,3}$ edges) measurements in points (1) 3YTZP ceramic grain and (2) FLG region.

3.2. Hardness and fracture propagation

The hardness values of the different composites are summarized in table 2. The results indicate that the addition of graphene-based nanostructures decreases the composites hardness with respect to the monolithic 3YTZP ceramic, disregarding the type of GBN added. The Vickers hardness also decreases with increasing GBN content, following the trend of composites with lower GNP content [10]. The same effect has been reported with different ceramic matrices as alumina [23,26] or SiAlON [27]. The results from nanoindentation (not performed on Z20G because of the high microstructural inhomogeneity observed in Z10G) correlate the hardness and Young's modulus with the homogeneity, content and type of GBN used. The Young's modulus decreases with increasing GBN homogeneity and content. The values of the instrumental hardness, which are systematically higher than those of conventional Vickers micro-hardness tests, follow the same trend as the Young's modulus. The decrease of hardness can be explained by a two-fold argument. In the first place, by the intrinsic properties of the graphene-based nanostructure, a much softer phase than the ceramic matrix (value of 1 GPa measured by nanoindentation [28]). Although the Young's modulus of graphene is extremely high (~1000 GPa), the graphene-based nanostructures are very easily

deformed under shear stress (parallel to their main ab plane) by the glide of the graphene layers with respect to each other, due to the weak Van der Waals interaction between them. In the second place, the GBNs placed between the ceramic grains favour grain boundary sliding and therefore plastic deformation of the composite. This mechanism was proposed to account for the hardness decrease in ZrO_2/GNP composites with GNP content higher than 0.05 wt% [29].

Table 2. Young's modulus, instrumental nano-hardness and Vickers hardness of the 3YTZP/GBN composites in this study. Data from the 3YTZP ceramic are included.

Sample	**E (GPa)**		**H_{Berk} (GPa)**		**H_V (GPa)**	
	in-plane	**cross-section**	**in-plane**	**cross-section**	**in-plane**	**cross-section**
3YTZP	263±5*		20.0±0.4*		13.9 ± 0.5	
Z10G	170 ± 30	188 ± 13	10 ± 3	11.0 ± 1.6	7.7 ± 2.2	8.5 ± 0.8
Z20G					spalling	4.6 ± 1.6
Z10F	100 ± 19	150 ± 16	8 ± 2	9 ± 1.7	5.3 ± 0.5	6.1 ± 0.3
Z20F	60 ± 6	72 ± 14	2.9 ± 0.7	4.2 ± 1.6	spalling	2.2 ± 0.2

*Data from a similar 3YTZP from the same powder as in this study, SPSed at 1350°C, with 99.4% relative density, 0.177±0.014 μm reported grain size and 14.21±0.09 GPa Vickers hardness[30].

Systematically higher values of elastic moduli and hardness are obtained in the cross sections as a consequence of the microstructural anisotropy of the material, also reported in composites with lower GNP content [10] or with other carbon nanostructures as fillers, such as carbon nanotubes [31,32]. The higher hardness values are obtained when the indentation load is applied on the plane parallel to the sintering axis, in agreement with the observations in bulk sintered graphene flakes [33]. The lower hardness values, when the load is applied on the composite in-plane surfaces, can be attributed to microscopic mechanisms with lower activation energy such as delamination and sliding of the graphene layers. The delamination of the graphene layers sometimes causes spalling which affects the indentation borders, impeding the correct formation of the indentation imprint, as it happened to the composites with 20 vol% GBN content, both with FLG and GNP.

The composites with FLG show lower hardness values with also lower standard deviations than the composites with GNP. The reduced hardness is due to the lower density in the composites with FLG and to the increased microstructural homogeneity. The FLG can be found less aggregated and in a higher percentage of ceramic grain boundaries than the GNP in their composites, facilitating deformation by grain boundary sliding in larger areas of the composite. The smaller standard deviation of the hardness values is also an indicator of the better homogeneity of the composite microstructure. The composites with GNP, on the other hand, present GNP-free well-defined ceramic areas similar in size to the imprint that are harder than the rest of the composite. This gives place to a larger dispersion of the results**.**

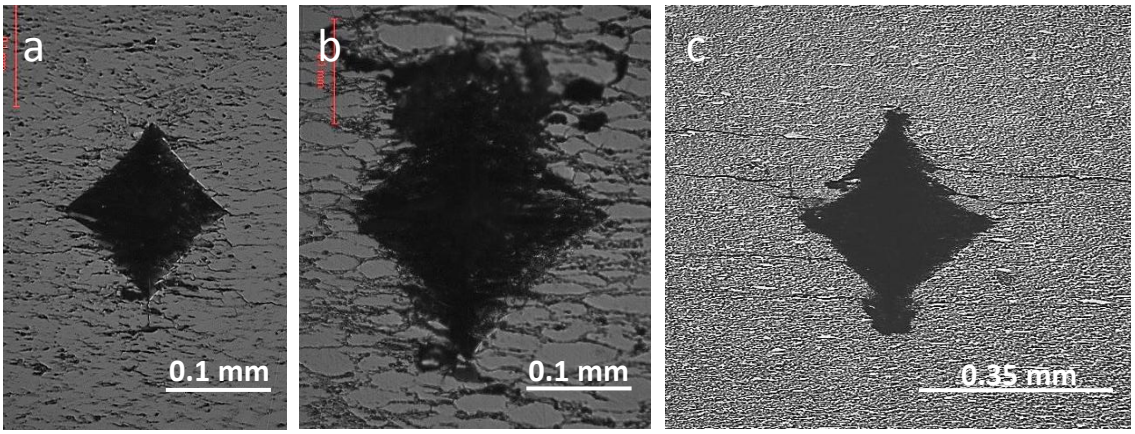

Figure 10. Optical micrographs of the composite cross sections after Vickers indentation at 10 kp showing (a) Z10G, (b) Z20G with extensive spalling and (c) Z20F with horizontal anisotropic crack propagation.

The application of high indentation loads (10 kp) to create fractures in the cross section of the composites has revealed some interesting additional facts. The composites with highest GNP content show an extensive spalling, probably due to the delamination of interconnected aggregated graphene-based nanostructures (figure 10b). The spalling is much less noticeable for the composites with FLG, since these multilayer graphene structures are smaller and better distributed through the ceramic matrix. In pure zirconia, as a typical fragile material, cracks arise only from the vertices of the indentation, two horizontal and two vertical ones. So indeed there are two significant differences between the monolithic ceramic and the composite with FLG: i. Anisotropy in the crack propagation and ii. Extensive microcracking. Usually, extensive microcracking around an indentation is considered

as an energy dissipating mechanism that could enhance fracture toughness, and it has been observed in composites with other ceramic matrices (for instance, silicon nitride [3]) and graphene nanosheets.

Regarding, the anisotropy, the cracks arising from the indentation imprints at high loads in these composites propagate on the surfaces of the FLG main ab planes. Thus, the FLG induce a crack deflection mechanism inhibiting crack propagation in the direction of the sintering axis, as can be observed in figure 10c. This result is in agreement with the TEM observations of the 3YTZP/FLG interface in these composites (fig. 8), which confirm the good interfacial bonding between both phases, even with the formation of an intermediate compound in the grain boundaries, and the low degree of stacking of these nanostructures forming thin groups of FLG which can be much better distributed through the ceramic grain boundaries. Very recently, it has been observed in Si_3N_4 nanocomposites with reduced graphene oxide (rGO) [34] that crack bridging is more effective when the reinforcement consists of large stacks of platelets with strong bonding to the matrix and high aspect ratios. Deeper and more systematic studies on crack propagation would be necessary to give an insight into the reinforcing mechanisms of FLG and GNPs in a 3YTZP matrix.

3.3. Electrical conductivity at room temperature.

The results of the measured electrical conductivity in the two relevant directions (parallel and perpendicular to the sintering axis) of the composites are shown in table 3.

Table 3. Electrical conductivity values of the composites in this study measured in the directions parallel and perpendicular to the compression axis during sintering.

Sample	**GBN filler**		Electrical conductivity, σ (Sm^{-1})	
	type	**Vol %**	**$\sigma_{\parallel}$**	**$\sigma_{\perp}$**
Z10G	GNP	10	16 ± 1	239 ± 6
Z10F	FLG	10	85 ± 3	790 ± 20
Z20G	GNP	20	544 ± 7	2740 ± 60
Z20F	FLG	20	480 ± 70	3400 ± 500

There is a noticeable increase of the electrical conductivity with the amount of GBN added to the ceramic matrix, of one order of magnitude in both measured directions when increasing the GBN content from 10 to 20 vol%. Regarding the anisotropy effects in the composites, the conductivity in the perpendicular direction to the compression axis during sintering, $\sigma_{\perp}$, is systematically higher than in the parallel direction, $\sigma_{\parallel}$ (also one order of magnitude). This electrical anisotropy is a direct consequence of the structural anisotropy detected in the composites, since the preferential orientation of the graphene platelets perpendicular to the compression axis during SPS means that in the configuration for measuring $\sigma_{\perp}$, the electric current flows mainly through the surface of the graphene nanosheets, which are often interconnected as observed by electron microscopy. In the parallel configuration, however, the current flows mainly through the c-axis of the graphene based sheets, finding larger ceramic isolating regions between the GBN and thus following a more tortuous path. If we focus on the differences of electrical conductivity due to the different fillers used, we can see that for 10 vol% GBN content, $\sigma_{\parallel}$ and $\sigma_{\perp}$ are five and three times higher for composites with FLG, respectively. For 20 vol% $\sigma_{\parallel}$ are practically identical for FLG and GNP while $\sigma_{\perp}$ is only 1.24 times higher for FLG. The reason for the improved electrical conductivity of the composites with FLG is twofold. In the first place, it is well known that the conductivity of the multilayer graphene decreases when the number of graphene layers increase, so the conductivity of the FLG is higher than that of the GNPs. In the second place, the composites with FLG show a better microstructural homogeneity, with a better percolated FLG network than in the case of composites with GNP.

Shin and Hong obtained an electrical conductivity value of 1.2 10^4 S/m for 4.1 vol% rGO in a YSZ matrix also sintered by SPS [9], values which are significantly higher than ours. They measured with a 4 probe technique but did not specify the current flow direction, presumably $\sigma_{\perp}$ due to the measuring technique. However, the values found by these authors are much higher than the values obtained by the scientific community for a variety of different ceramic matrices with rGO and graphene nanoplatelets, as can be seen in a comprehensive review by Miranzo et al. [35].

The $\sigma_{\perp}$, value for the composite with 10 vol% FLG content in this study is higher than those for composites with AlN [36] or Si_3N_4 [18] matrix, despite using the same GBN content. However, in these studies, thicker graphene nanoplatelets were used as fillers.

On the other hand, this value is lower than the published one for composites with AlN matrix with thinner graphene nanosheets (GNS) [37], probably due to the lower number of graphene layers in these nanostructures. The composites with 20 vol% FLG in this study have a $\sigma_{\perp,}$ in the same order than those of composites with Si_3N_4 [18] and SiC [16] matrix, for the same GNP content.

The conductivity values achieved by the composites in this study, especially those with GNPs have as an upper limit the properties of graphite, which is considered to be a good electric conductor along the ab basal plane, with a conductivity value of (20-40) 10^4 Sm^{-1}, whereas in the perpendicular direction the conductivity falls to 0.03 10^4 S m^{-1} [38] .

4. Conclusions

In this work, the influence of using different contents of graphene-based fillers differing in the number of layers (FLG with n~3 and GNP with n~150 layers) in a 3YTZP ceramic matrix has been assessed.

The common facts in the dense sintered composites are the structural preservation of the graphene-based nanostructures, the anisotropy due to their preferential orientation, the sub micrometric round-shaped ceramic grains and the presence of crystalline and amorphous interfaces 3YTZP/GBN. Also, the formation of an intermediate zirconia oxycarbide in some interfaces, suggesting a good interfacial bonding which would favor load transfer between the ceramic matrix and the filler.

There are also remarkable differences between the composites with the two GBN used. While most grouped GNPs pull-outs appear as rigid structures much larger than the ceramic grains, the FLG is much more flexible, less aggregated, thinner and similar in size to the ceramic 3YTZP grains. The FLG is found interconnected at grain boundaries surrounding groups of ceramic grains, with a slight FLG stacking of 2-5 nanosheets and much more homogeneously distributed in the ceramic matrix than the GNPs.

The few layered GBN, due to their higher specific surface area, is more effective in reducing the ceramic grain size and also reducing densification of the composites at

high concentrations. The FLG interplanar spacing estimated by TEM, larger than the GNPs spacing, can contribute to the lower density of the composites with FLG.

The Young's modulus, hardness and instrumental nano-hardness decrease with increasing GBN content and with improved GBN dispersion, in correlation with the density values.

The incorporation of FLG to a zirconia matrix greatly inhibits the crack propagation that occurs perpendicular to their preferential orientation plane, with an efficient crack deflection mechanism, due to a better distribution of the thinner FLG in the ceramic grain boundaries that allows an improved load transfer.

The composites with thinner GBN (FLG) have higher electrical conductivity than those with GNP and all the composites are electrically anisotropic. The maximum value was achieved for the composite with 20 vol% FLG, $\sigma_{\perp}$= 3400 ± 500 Sm^{-1}, in the direction perpendicular to the compression axis during sintering, due to the higher conductivity of the FLG with smaller number of layers and to their better dispersion in the ceramic matrix.

Acknowledgments

The authors would like to acknowledge the financial support provided by the Spanish Ministry (Ministerio de Economía y Competitividad) with the project MAT2015-67889-P, co-funded by European FEDER and the research facilities of CITIUS (Univ. Sevilla): XRD, SEM and microanalysis, and those at ICMS (CSIC): Raman spectroscopy and TEM.

References

[1] C. Lee, X. Wei, J.W. Kysar, J. Hone, Measurement of the elastic properties and intrinsic strength of monolayer graphene - Supplementary Information, Science. 321 (2008) 385–8. doi:10.1126/science.1157996.

[2] L.S. Walker, V.R. Marotto, M.A. Rafiee, N. Koratkar, E.L. Corral, Toughening in Graphene Ceramic Composites, ACS Nano. 5 (2011) 3182–3190. doi:10.1021/nn200319d.

[3] C. Ramirez, P. Miranzo, M. Belmonte, M. Isabel Osendi, P. Poza, S.M. Vega-Diaz, M. Terrones, Extraordinary toughening enhancement and flexural strength in Si3N4 composites using graphene sheets, J. Eur. Ceram. Soc. 34 (2014) 161–169. doi:10.1016/j.jeurceramsoc.2013.08.039.

[4] G.B. Yadhukulakrishnan, S. Karumuri, A. Rahman, R.P. Singh, A. Kaan Kalkan, S.P. Harimkar, Spark plasma sintering of graphene reinforced zirconium diboride ultra-high temperature ceramic composites, Ceram. Int. 39 (2013) 6637–6646. doi:http://dx.doi.org/10.1016/j.ceramint.2013.01.101.

[5] P. Miranzo, C. Ramirez, B. Roman-Manso, L. Garzon, H.R. Gutierrez, M. Terrones, C. Ocal, M. Isabel Osendi, M. Belmonte, In situ processing of electrically conducting graphene/SiC nanocomposites, J. Eur. Ceram. Soc. 33 (2013) 1665–1674. doi:10.1016/j.jeurceramsoc.2013.01.021.

[6] S.J. Wang, Y. Geng, Q. Zheng, J.-K. Kim, Fabrication of highly conducting and transparent graphene films, Carbon N. Y. 48 (2010) 1815–1823.

[7] A. Centeno, V.G.G. Rocha, B. Alonso, A. Fernández, C.F.F. Gutierrez-Gonzalez, R. Torrecillas, A. Zurutuza, Graphene for tough and electroconductive alumina ceramics, J. Eur. Ceram. Soc. 33 (2013) 3201–3210. doi:http://dx.doi.org/10.1016/j.jeurceramsoc.2013.07.007.

[8] F. Chen, D. Jin, K. Tyeb, B. Wang, Y.-H. Han, S. Kim, J.M. Schoenung, Q. Shen, L. Zhang, Field assisted sintering of graphene reinforced zirconia ceramics, Ceram. Int. 41 (2015) 6113–6116.

[9] J.-H. Shin, S.-H. Hong, Fabrication and properties of reduced graphene oxide reinforced yttria-stabilized zirconia composite ceramics, J. Eur. Ceram. Soc. 34 (2014) 1297–1302. doi:10.1016/j.jeurceramsoc.2013.11.034.

[10] A. Gallardo-López, I. Márquez-Abril, A. Morales-Rodríguez, A. Muñoz, R. Poyato, Dense Graphene Nanoplatelet/Yttria Tetragonal Zirconia Composites: Processing, Hardness and Electrical Conductivity, Ceram. Int. 43 (2017) 11743–

11752. doi:10.1016/j.ceramint.2017.06.007.

[11] Y. Gaillard, E. Jiménez-Piqué, F. Soldera, F. Mücklich, M. Anglada, Quantification of hydrothermal degradation in zirconia by nanoindentation, Acta Mater. 56 (2008) 4206–4216.

[12] W.C. Oliver, G.M. Pharr, An improved technique for determining hardness and elastic modulus using load and displacement sensing indentation experiments, J. Mater. Res. 7 (1992) 1564–1583.

[13] Q. Li, J. Song, F. Besenbacher, M. Dong, Two-dimensional material confined water, Acc. Chem. Res. 48 (2014) 119–127.

[14] C. Ramirez, M. Isabel Osendi, Characterization of graphene nanoplatelets-Si3N4 composites by Raman spectroscopy, J. Eur. Ceram. Soc. 33 (2013) 471–477. doi:10.1016/j.jeurceramsoc.2012.09.014.

[15] F. Inam, T. Vo, B.R. Bhat, Structural stability studies of graphene in sintered ceramic nanocomposites, Ceram. Int. 40 (2014) 16227–16233. doi:10.1016/j.ceramint.2014.07.058.

[16] B. Román-Manso, E. Domingues, F.M. Figueiredo, M. Belmonte, P. Miranzo, Enhanced electrical conductivity of silicon carbide ceramics by addition of graphene nanoplatelets, J. Eur. Ceram. Soc. 35 (2015) 2723–2731. doi:10.1016/j.jeurceramsoc.2015.03.044.

[17] A.C. Ferrari, Raman spectroscopy of graphene and graphite: Disorder, electron–phonon coupling, doping and nonadiabatic effects, Solid State Commun. 143 (2007) 47–57. doi:10.1016/j.ssc.2007.03.052.

[18] C. Ramirez, F.M. Figueiredo, P. Miranzo, P. Poza, M.I. Osendi, M. Isabel Osendi, Graphene nanoplatelet/silicon nitride composites with high electrical conductivity, Carbon N. Y. 50 (2012) 3607–3615. doi:10.1016/j.carbon.2012.03.031.

[19] O. Tapasztó, L. Tapasztó, H. Lemmel, V. Puchy, J. Dusza, C. Balázsi, K. Balázsi, High orientation degree of graphene nanoplatelets in silicon nitride composites prepared by spark plasma sintering, Ceram. Int. 42 (2016) 1002–1006.

[20] M. Michalkova, M. Kasiarova, P. Tatarko, J.J. Dusza, P. Sajgalik, M. Michálková, M. Kašiarová, P. Tatarko, J.J. Dusza, P. Šajgalík, Effect of homogenization treatment on the fracture behaviour of silicon nitride/graphene nanoplatelets composites, J. Eur. Ceram. Soc. 34 (2014) 3291–3299. doi:10.1016/j.jeurceramsoc.2014.03.023.

[21] C. López-Pernía, C. Muñoz-Ferreiro, C. González-Orellana, A. Morales-Rodríguez, Á. Gallardo-López, R. Poyato, Optimizing the homogenization technique for graphene nanoplatelet/yttria tetragonal zirconia composites: Influence on the microstructure and the electrical conductivity, J. Alloys Compd. 767 (2018) 994–1002.

[22] I. Ahmad, T. Subhani, N. Wang, Y. Zhu, Thermophysical Properties of High-Frequency Induction Heat Sintered Graphene Nanoplatelets/Alumina Ceramic Functional Nanocomposites, J. Mater. Eng. Perform. (n.d.) 1–11.

[23] Y. Fan, M. Estili, G. Igarashi, W. Jiang, A. Kawasaki, The effect of homogeneously dispersed few-layer graphene on microstructure and mechanical properties of Al2O3 nanocomposites, J. Eur. Ceram. Soc. 34 (2014) 443–451. doi:10.1016/j.jeurceramsoc.2013.08.035.

[24] I. Ahmad, M. Islam, N.H. Alharthi, H. Alawadhi, T. Subhani, K.S. Munir, S.I. Shah, F. Inam, Y. Zhu, Chemical and structural analyses of the graphene nanosheet/alumina ceramic interfacial region in rapidly consolidated ceramic nanocomposites, J. Compos. Mater. 52 (2017) 417–428. doi:10.1177/0021998317708235.

[25] J. Wang, Z. Li, G. Fan, H. Pan, Z. Chen, D. Zhang, Reinforcement with graphene nanosheets in aluminum matrix composites, Scr. Mater. 66 (2012) 594–597.

[26] I. Ahmad, M. Islam, H.S. Abdo, T. Subhani, K.A. Khalil, A.A. Almajid, B. Yazdani, Y. Zhu, Toughening mechanisms and mechanical properties of graphene nanosheet-reinforced alumina, Mater. Des. 88 (2015) 1234–1243.

[27] A. Cinar, S. Baskut, A.T. Seyhan, S. Turan, Tailoring the properties of spark plasma sintered SiAlON containing graphene nanoplatelets by using different exfoliation and size reduction techniques: Anisotropic mechanical and thermal

properties, J. Eur. Ceram. Soc. (2017).

[28] A. Nieto, D. Lahiri, A. Agarwal, Synthesis and properties of bulk graphene nanoplatelets consolidated by spark plasma sintering, Carbon N. Y. 50 (2012) 4068–4077. doi:10.1016/j.carbon.2012.04.054.

[29] D.-T. Vu, Y.-H. Han, F. Chen, D. Jin, J.M. Schoenung, D.-Y. Lee, Graphene Nano-Platelets Reinforced ZrO2 Consolidated by Spark Plasma Sintering, Sci. Adv. Mater. 8 (2016) 312–317.

[30] L. Melk, J.J. Roa Rovira, F. García-Marro, M.-L. Antti, B. Milsom, M.J. Reece, M. Anglada, Nanoindentation and fracture toughness of nanostructured zirconia/multi-walled carbon nanotube composites, Ceram. Int. 41 (2015) 2453–2461. doi:10.1016/j.ceramint.2014.10.060.

[31] A. Gallardo-López, R. Poyato, A. Morales-Rodríguez, A. Fernández-Serrano, A. Muñoz, A. Domínguez-Rodríguez, Hardness and flexural strength of single-walled carbon nanotube/alumina composites, J. Mater. Sci. 49 (2014) 7116–7123. doi:10.1007/s10853-014-8419-5.

[32] R. Poyato, J. Macías-Delgado, A. García-Valenzuela, Á. Gallardo-López, A. Morales-Rodríguez, A. Muñoz, A. Domínguez-Rodríguez, T. Gallardo-López, A. Morales-Rodríguez, A. Muñoz, A. Domínguez-Rodríguez, Mechanical and electrical properties of low SWNT content 3YTZP composites, J. Eur. Ceram. Soc. 35 (2015) 2351–2359. doi:10.1016/j.jeurceramsoc.2015.02.022.

[33] C. Rudolf, B. Boesl, A. Agarwal, In situ indentation behavior of bulk multi-layer graphene flakes with respect to orientation, Carbon N. Y. 94 (2015) 872–878.

[34] C. Ramírez, Q. Wang, M. Belmonte, P. Miranzo, M.I. Osendi, B.W. Sheldon, N.P. Padture, Direct in situ observation of toughening mechanisms in nanocomposites of silicon nitride and reduced graphene-oxide, Scr. Mater. 149 (2018) 40–43.

[35] P. Miranzo, M. Belmonte, M.I. Osendi, From bulk to cellular structures: A review on ceramic/graphene filler composites, J. Eur. Ceram. Soc. 37 (2017) 3649–3672.

[36] I.N.G. Simsek, A. Nistal, E. García, D. Pérez-Coll, P. Miranzo, M.I. Osendi, The effect of graphene nanoplatelets on the thermal and electrical properties of aluminum nitride ceramics, J. Eur. Ceram. Soc. 37 (2017) 3721–3729.

[37] C. Yun, Y. Feng, T. Qiu, J. Yang, X. Li, L. Yu, Mechanical, electrical, and thermal properties of graphene nanosheet/aluminum nitride composites, Ceram. Int. 41 (2015) 8643–8649.

[38] H.O. Pierson, Handbook of carbon, graphite, diamonds and fullerenes: processing, properties and applications, William Andrew, 2012.

[39] R. Poyato, J. Osuna, A. Morales-Rodríguez, Á. Gallardo-López, Electrical conduction mechanisms in graphene nanoplatelet/yttria tetragonal zirconia composites, Ceram. Int. 44 (2018) 14610–14616. doi:10.1016/j.ceramint.2018.05.082.

Graphical Abstract (for review)

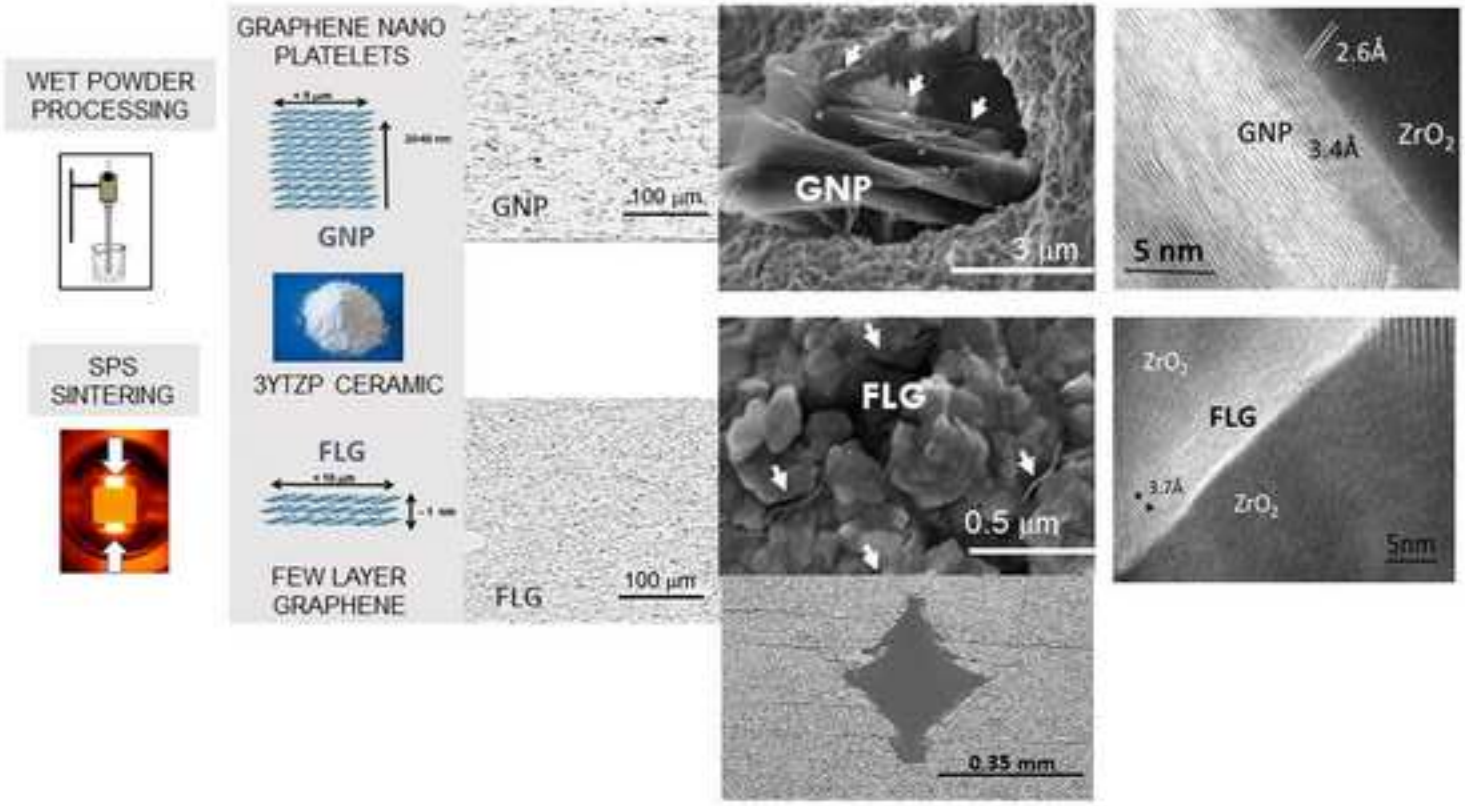

Highlights

- A high homogeneity was achieved in zirconia composites with few layer graphene.
- Crystalline and amorphous zirconia/graphene nanostructure interfaces coexistence.
- An intermediate zirconia oxycarbide detected in some grain boundaries.
- Few layer graphene inhibits crack propagation in the sintering pressing direction.
- Composites with few layer graphene show the highest electrical conductivity.

Table 3

Table 3. Electrical conductivity values of the composites in this study measured in the directions parallel and perpendicular to the compression axis during sintering.

Sample	***GBN filler***		*Electrical conductivity, σ (Sm^{-1})*	
	type	***Vol %***	$\sigma_{\parallel}$	$\sigma_{\perp}$
Z10G	*GNP*	*10*	*16 ± 1*	*239 ± 6*
Z10F	*FLG*	*10*	*85 ± 3*	*790 ± 20*
Z20G	*GNP*	*20*	*544 ± 7*	*2740 ± 60*
Z20F	*FLG*	*20*	*480 ± 70*	*3400 ± 500*

Figure 1a

Click here to download high resolution image

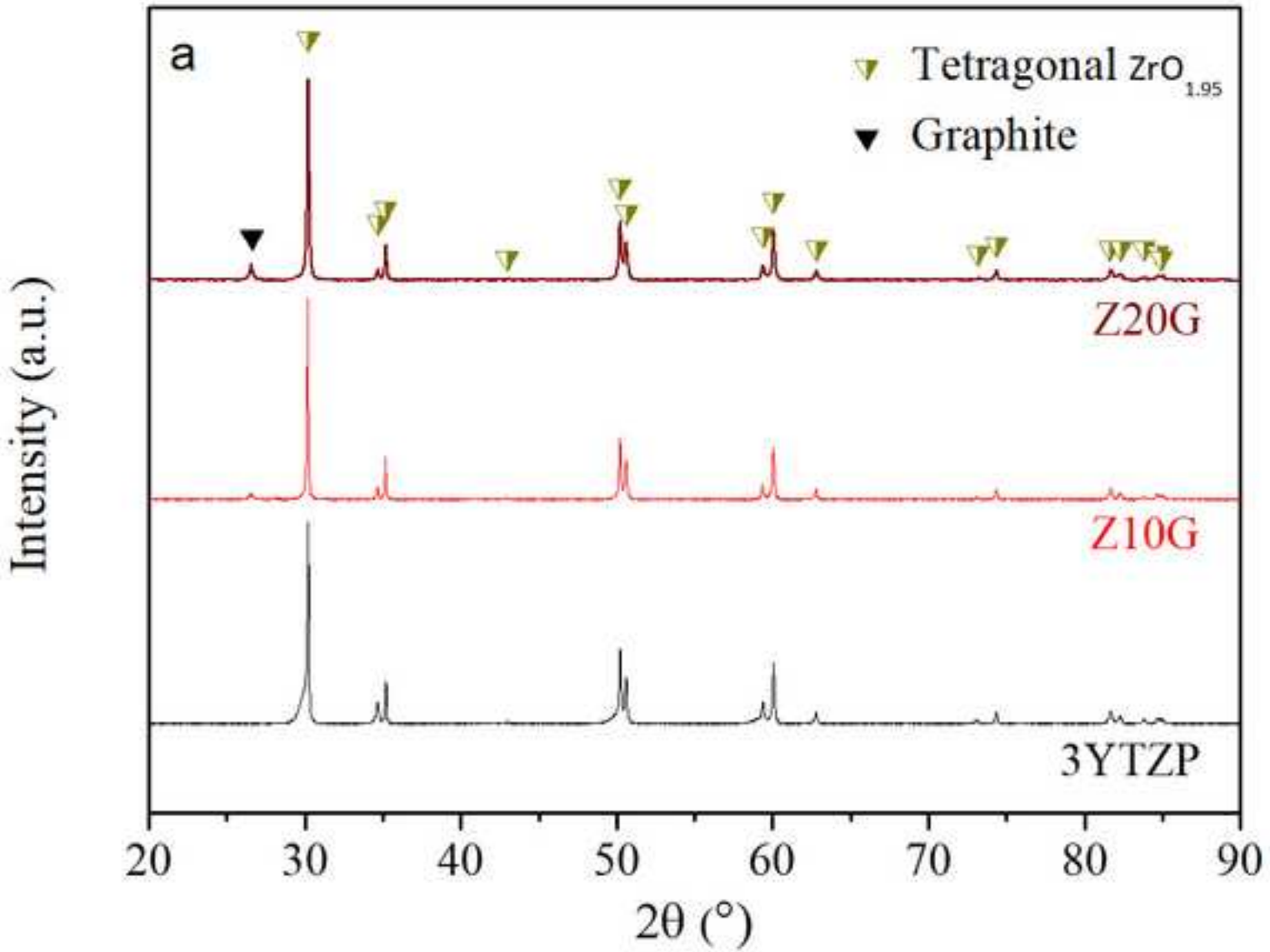

Figure 1b

Click here to download high resolution image

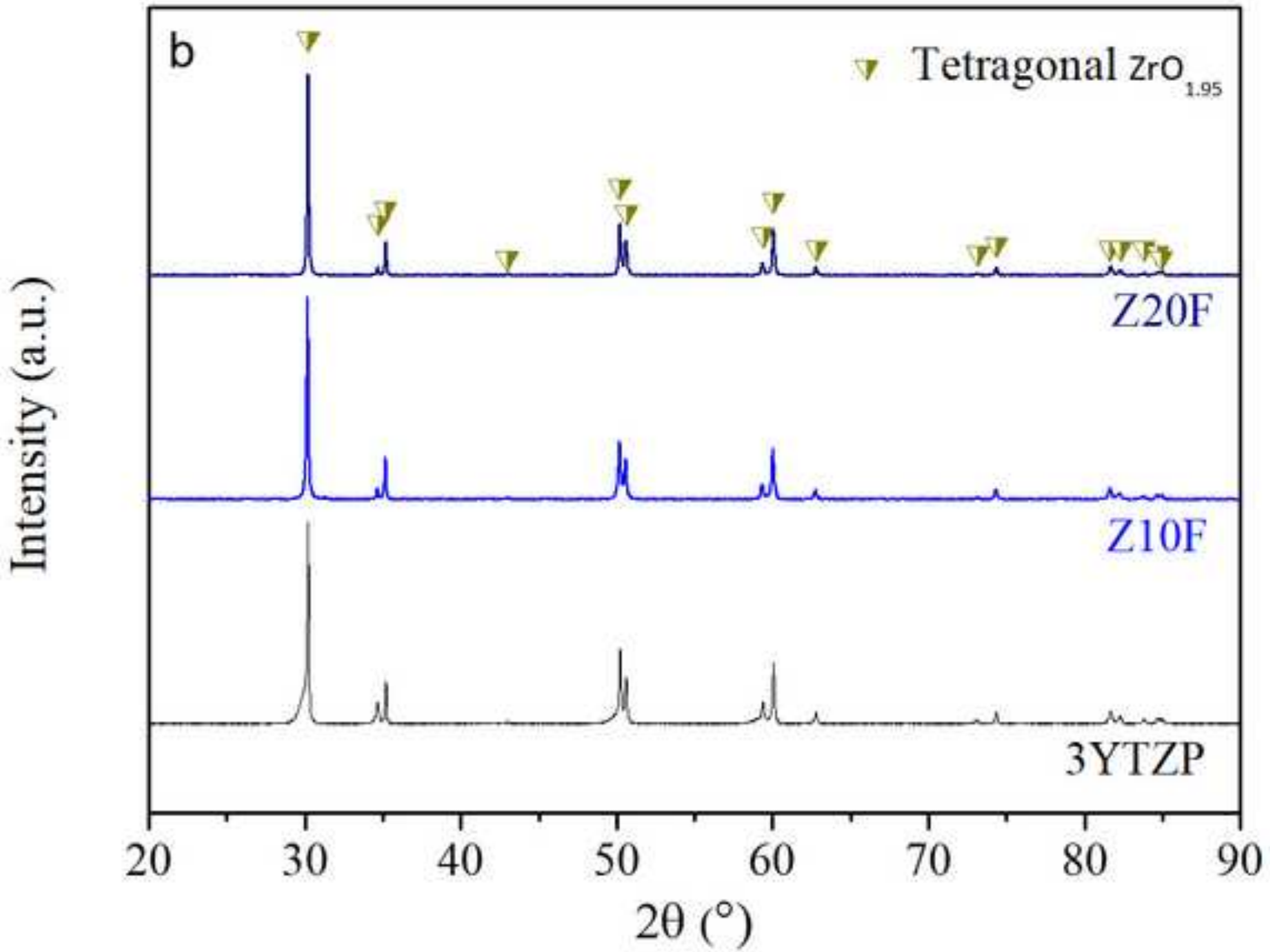

Figure 2a
Click here to download high resolution image

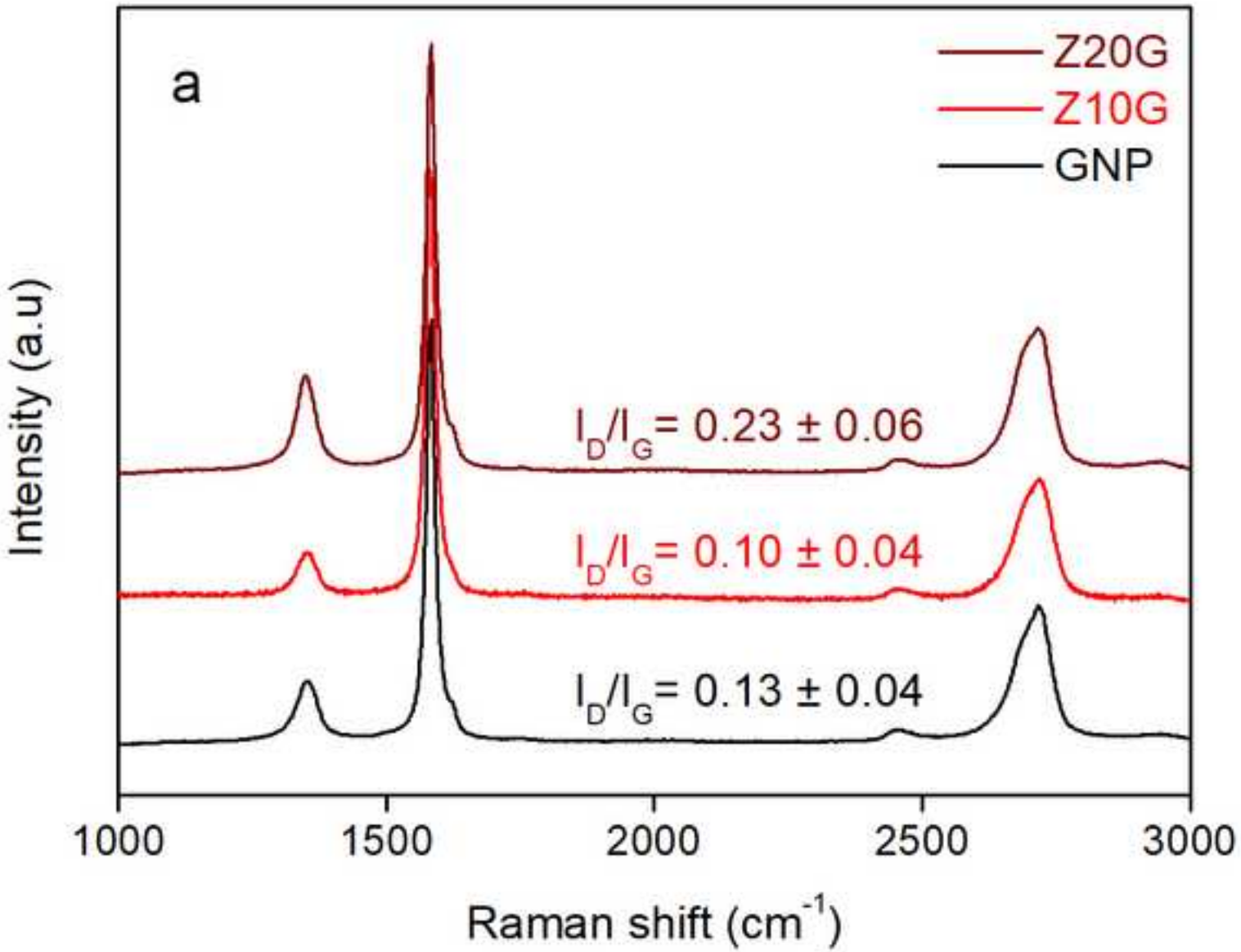

Figure 2b
Click here to download high resolution image

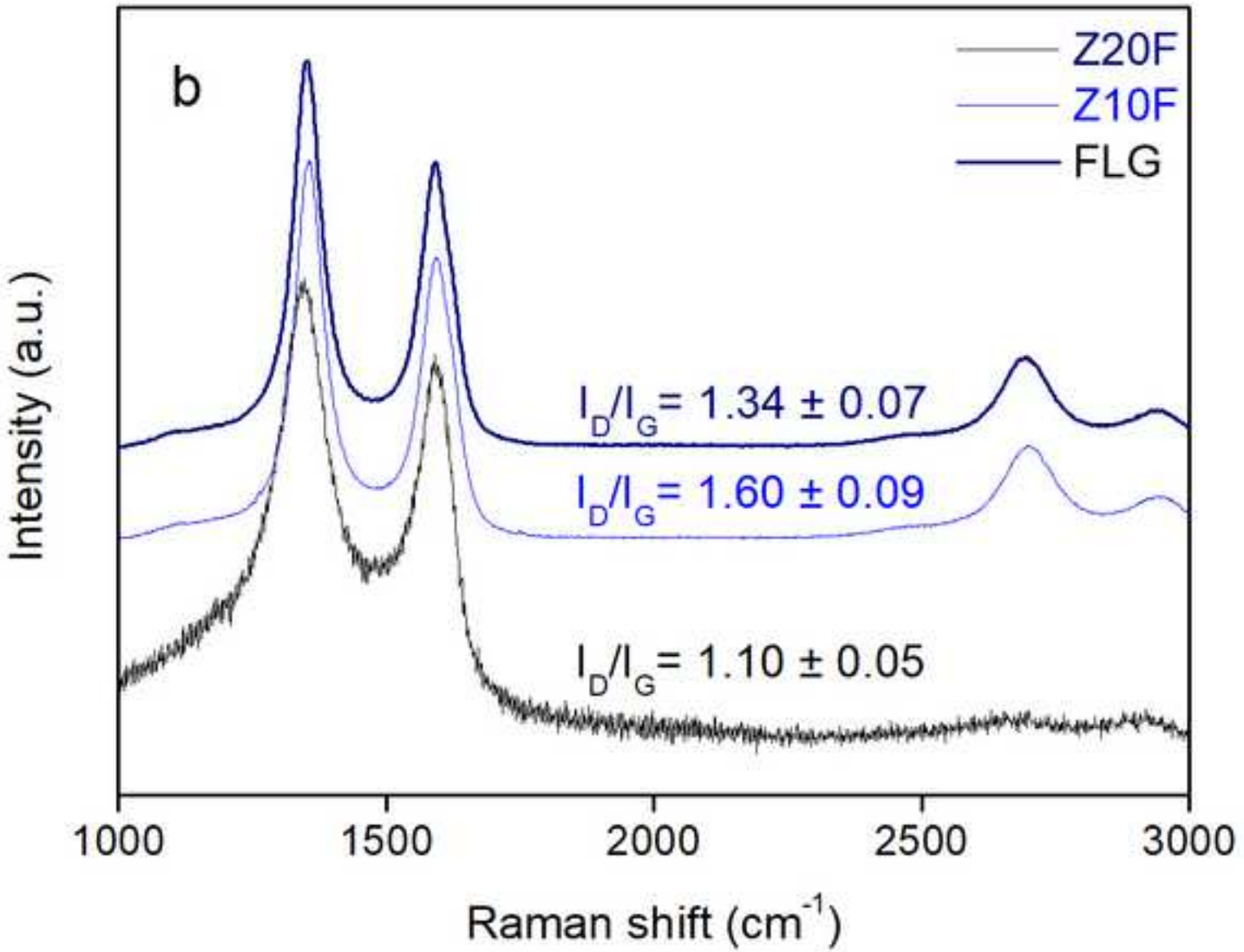

Figure 3ab

Click here to download high resolution image

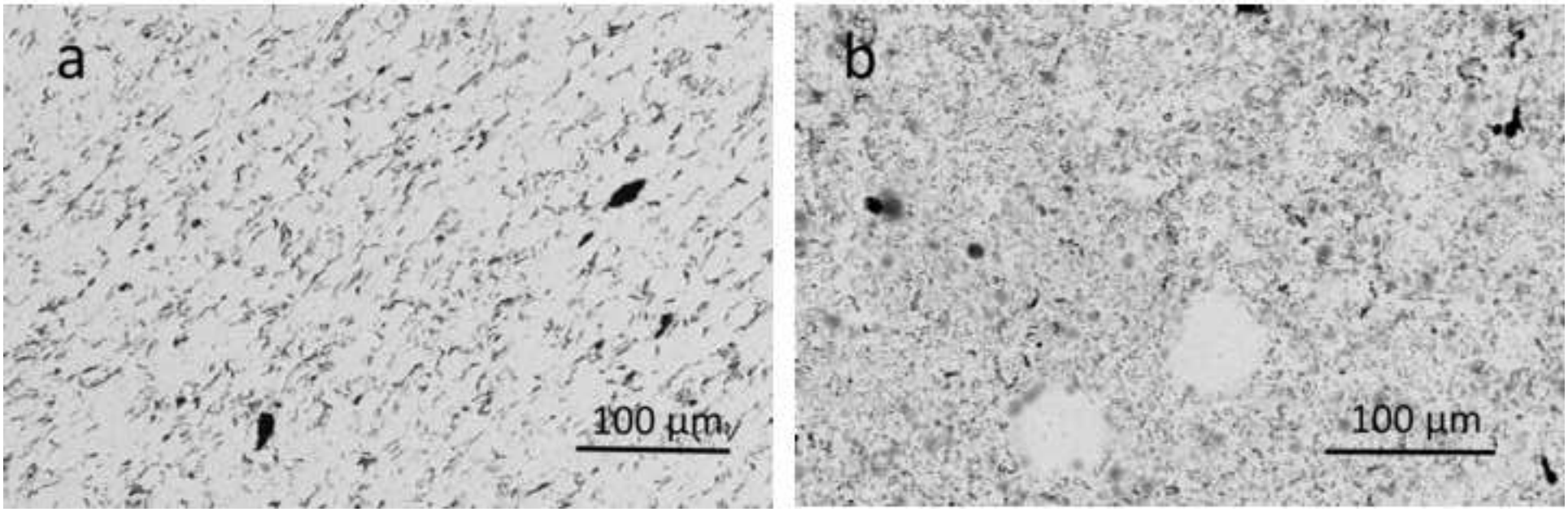

Figure 3cd

Click here to download high resolution image

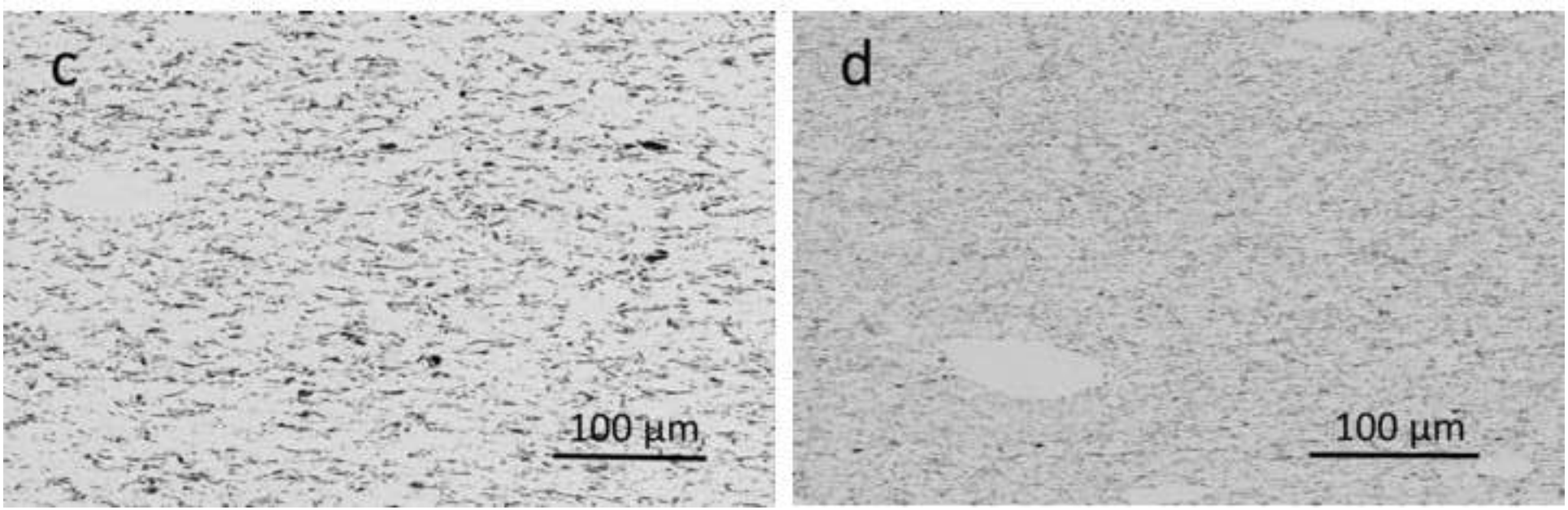

Figure 3ef

Click here to download high resolution image

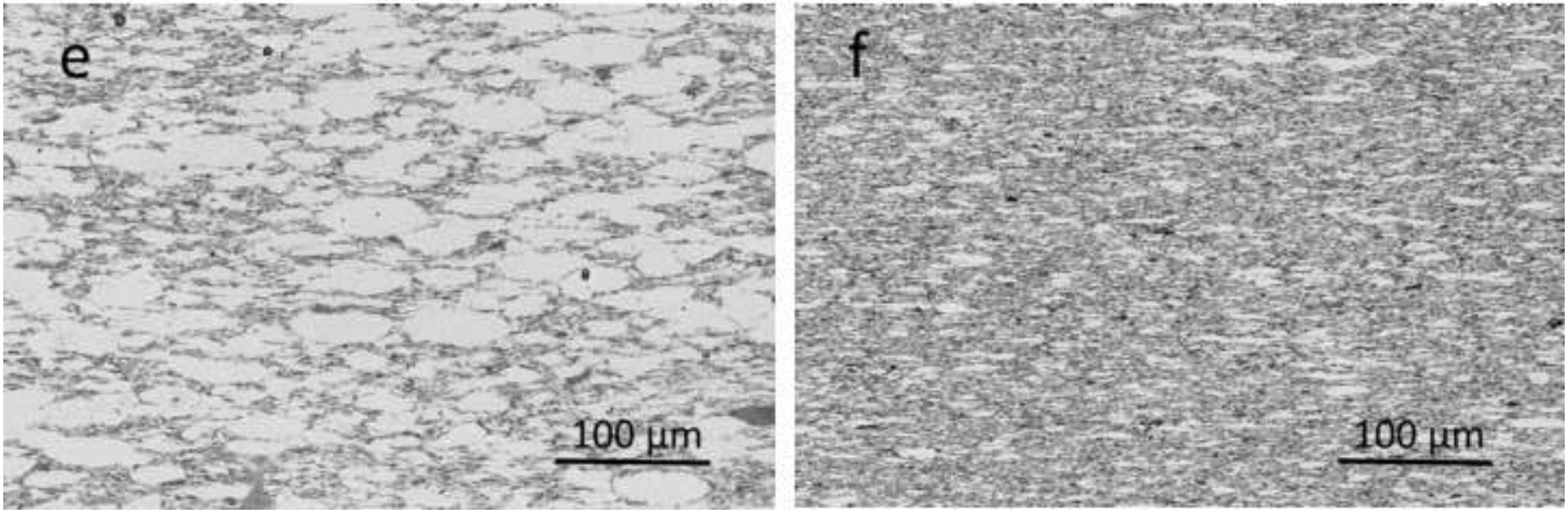

Figure 4

Click here to download high resolution image

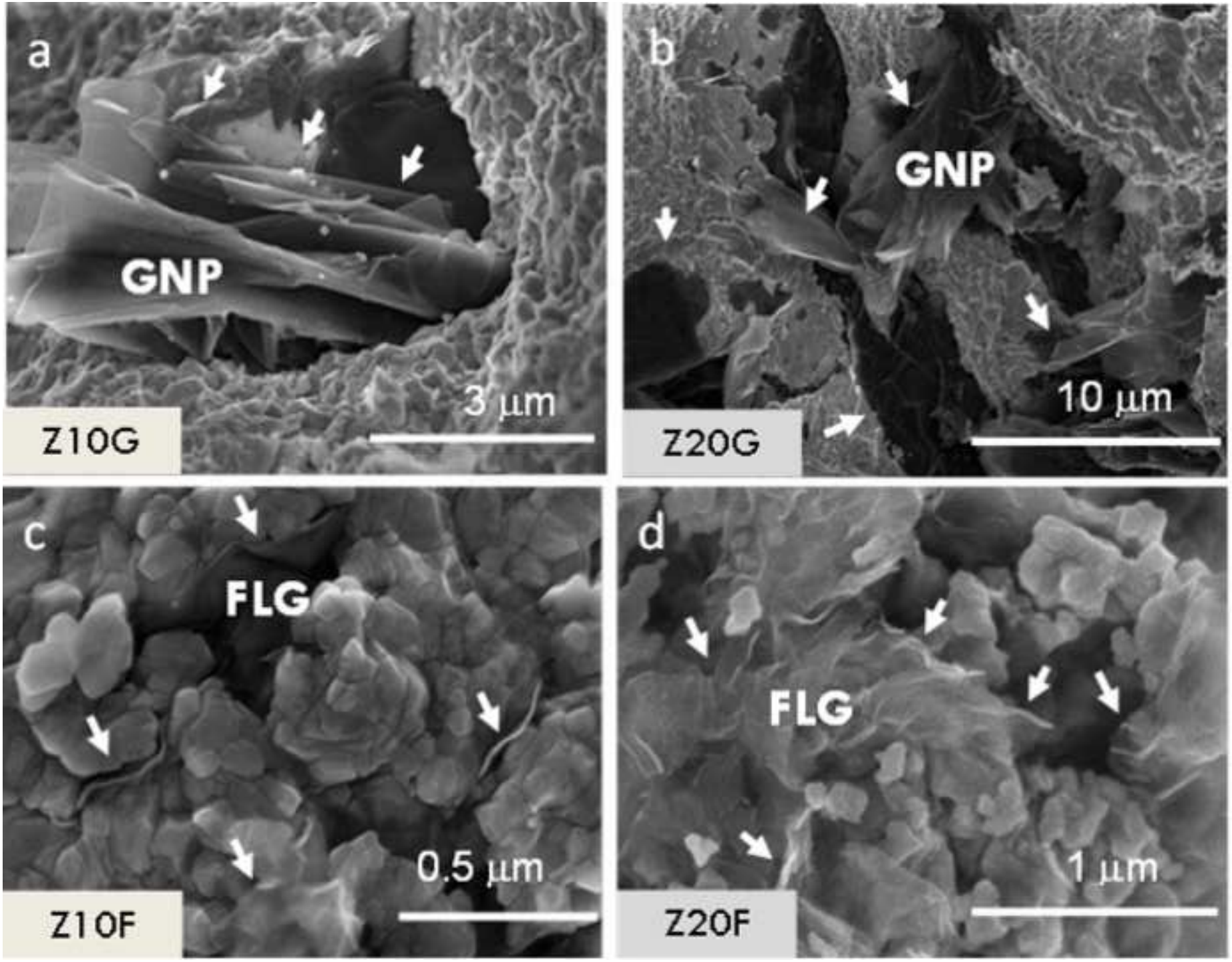

Figure 5

Click here to download high resolution image

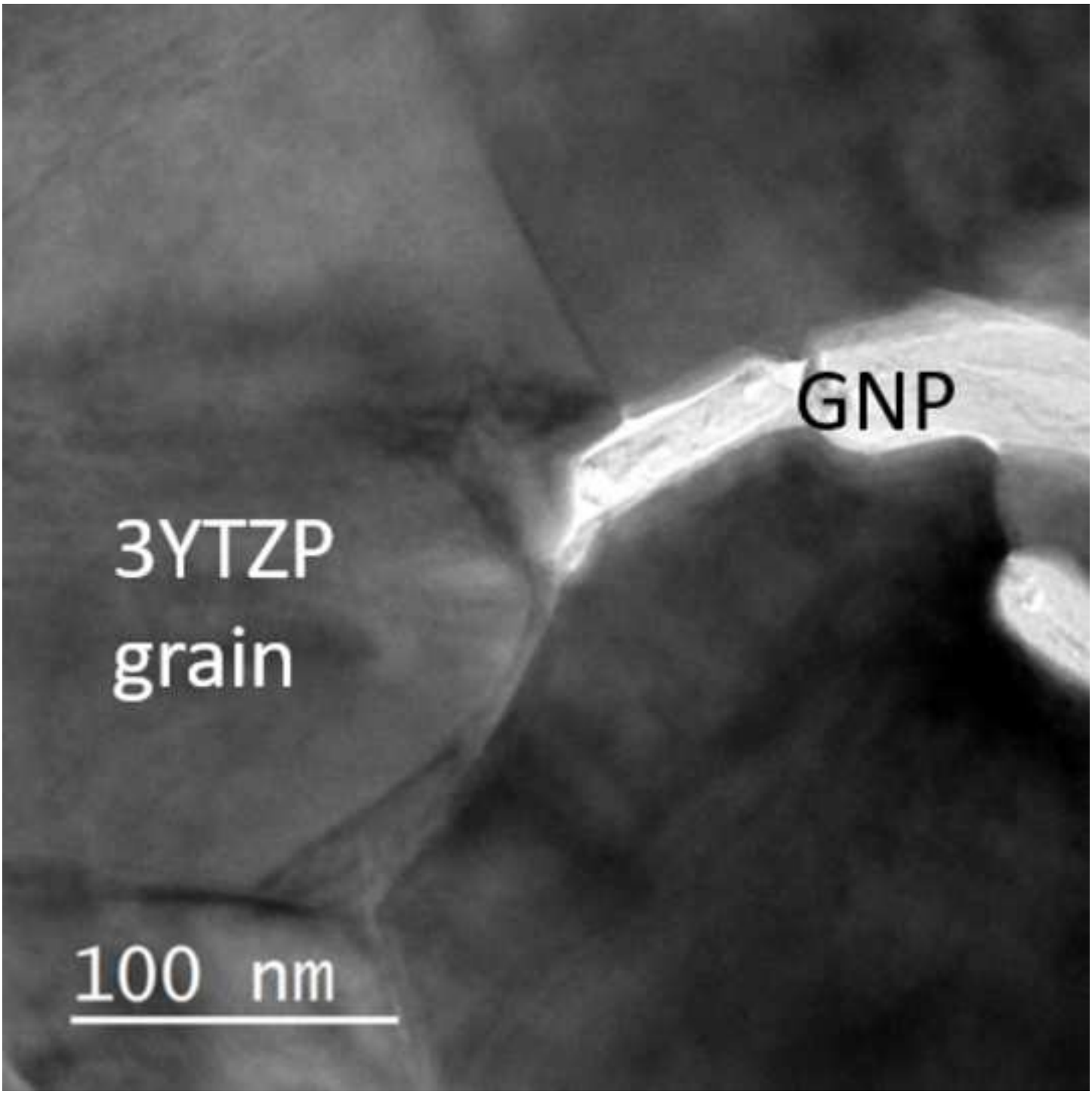

Figure 6

Click here to download high resolution image

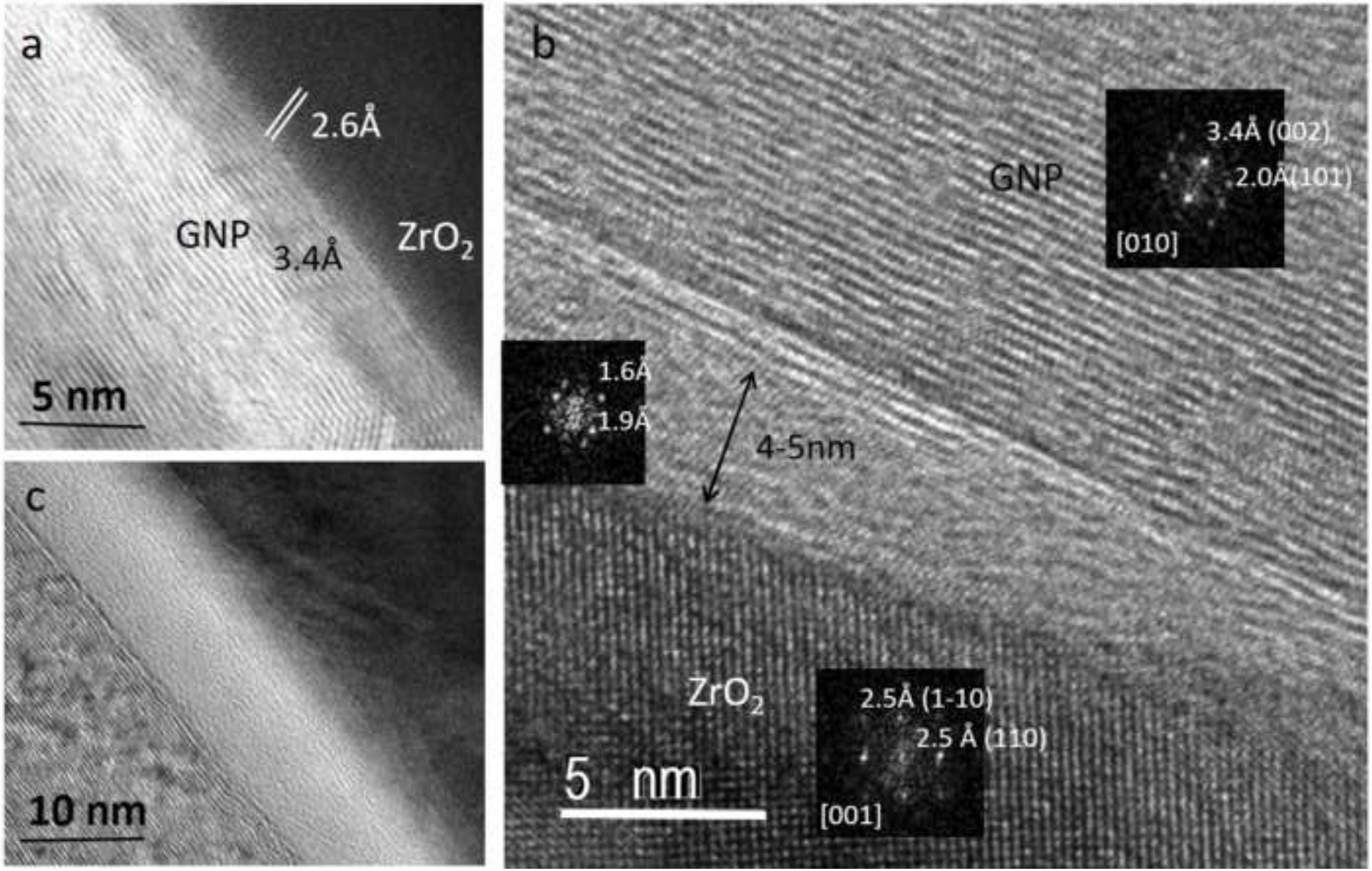

Figure 7a

Click here to download high resolution image

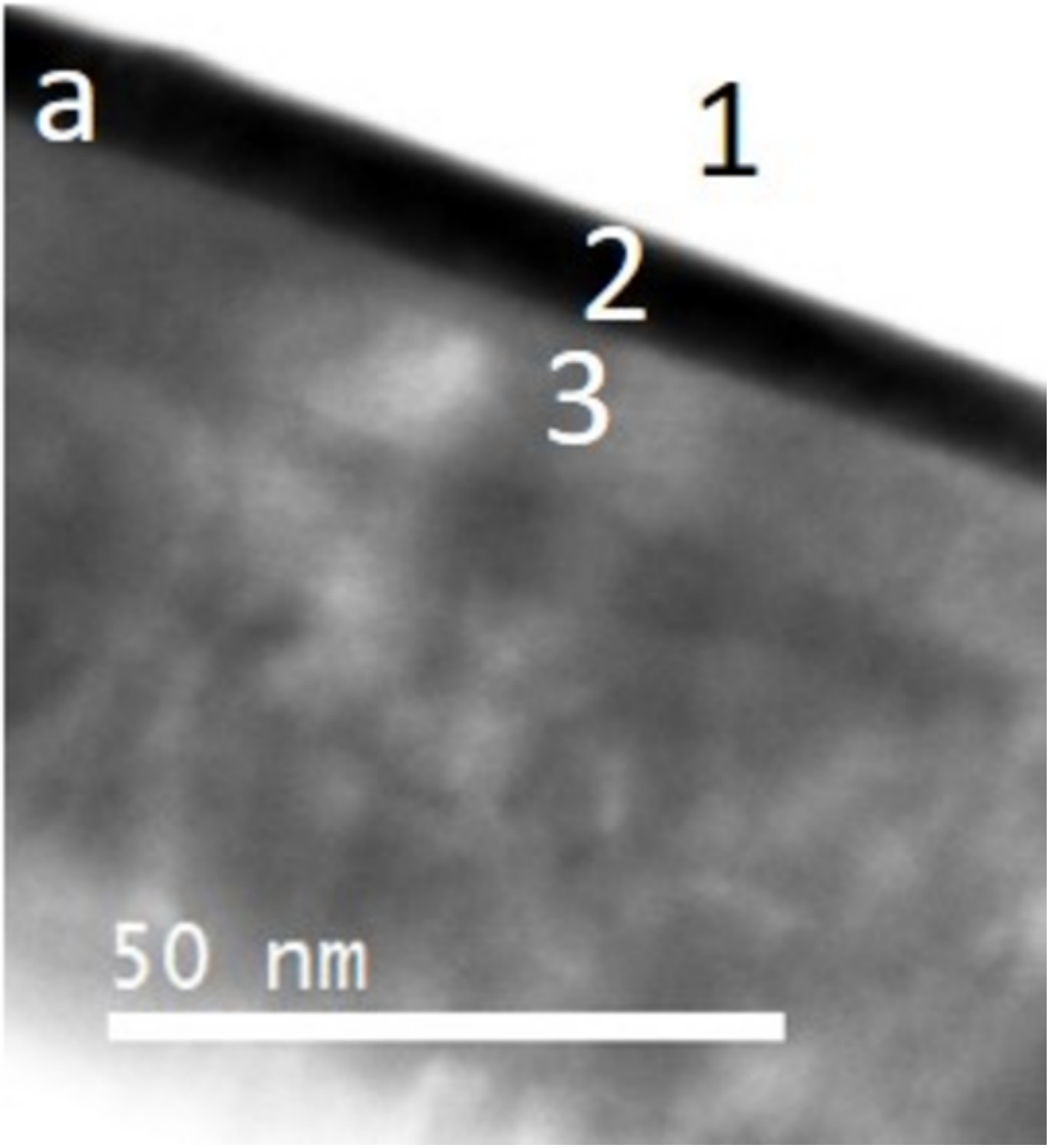

Figure 7b

Click here to download high resolution image

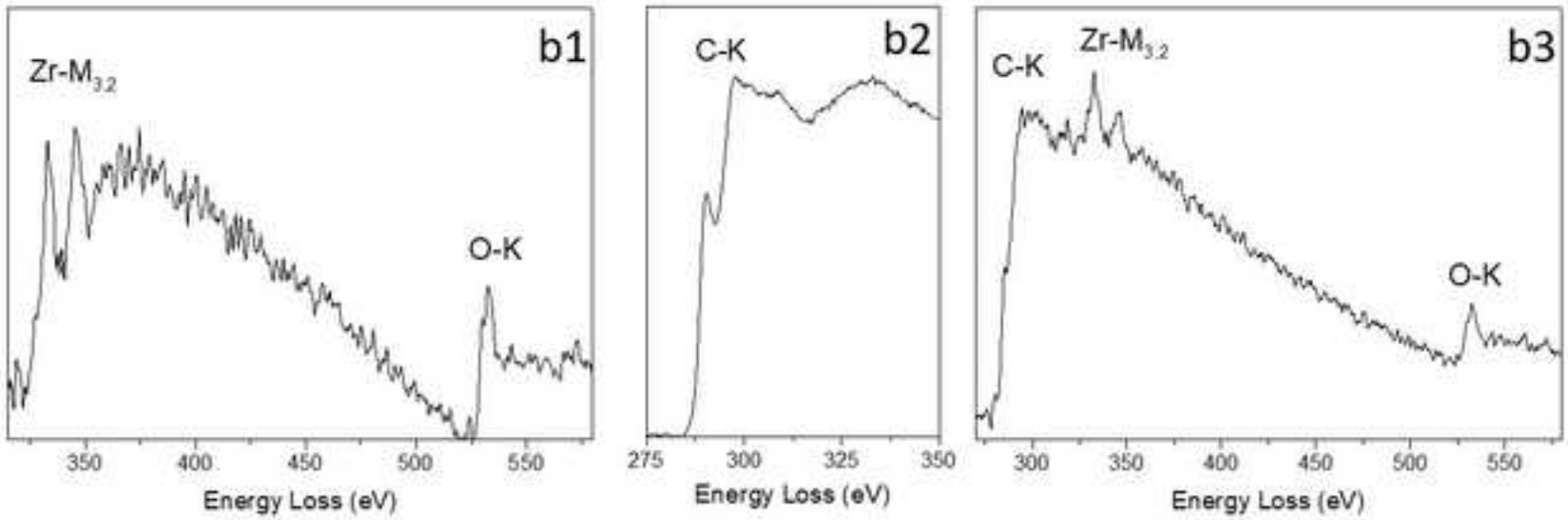

Figure 8a

Click here to download high resolution image

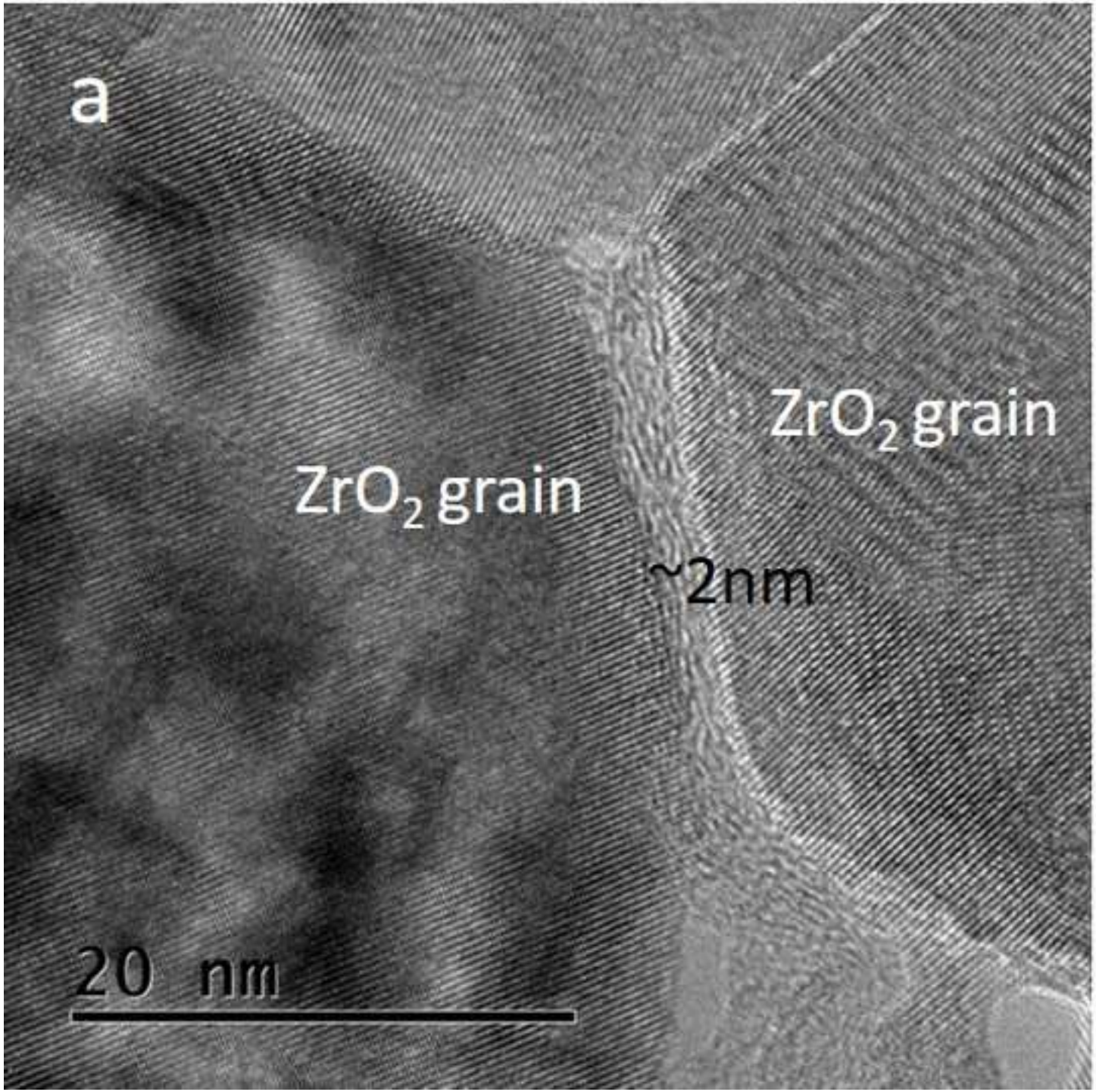

Figure 8b

Click here to download high resolution image

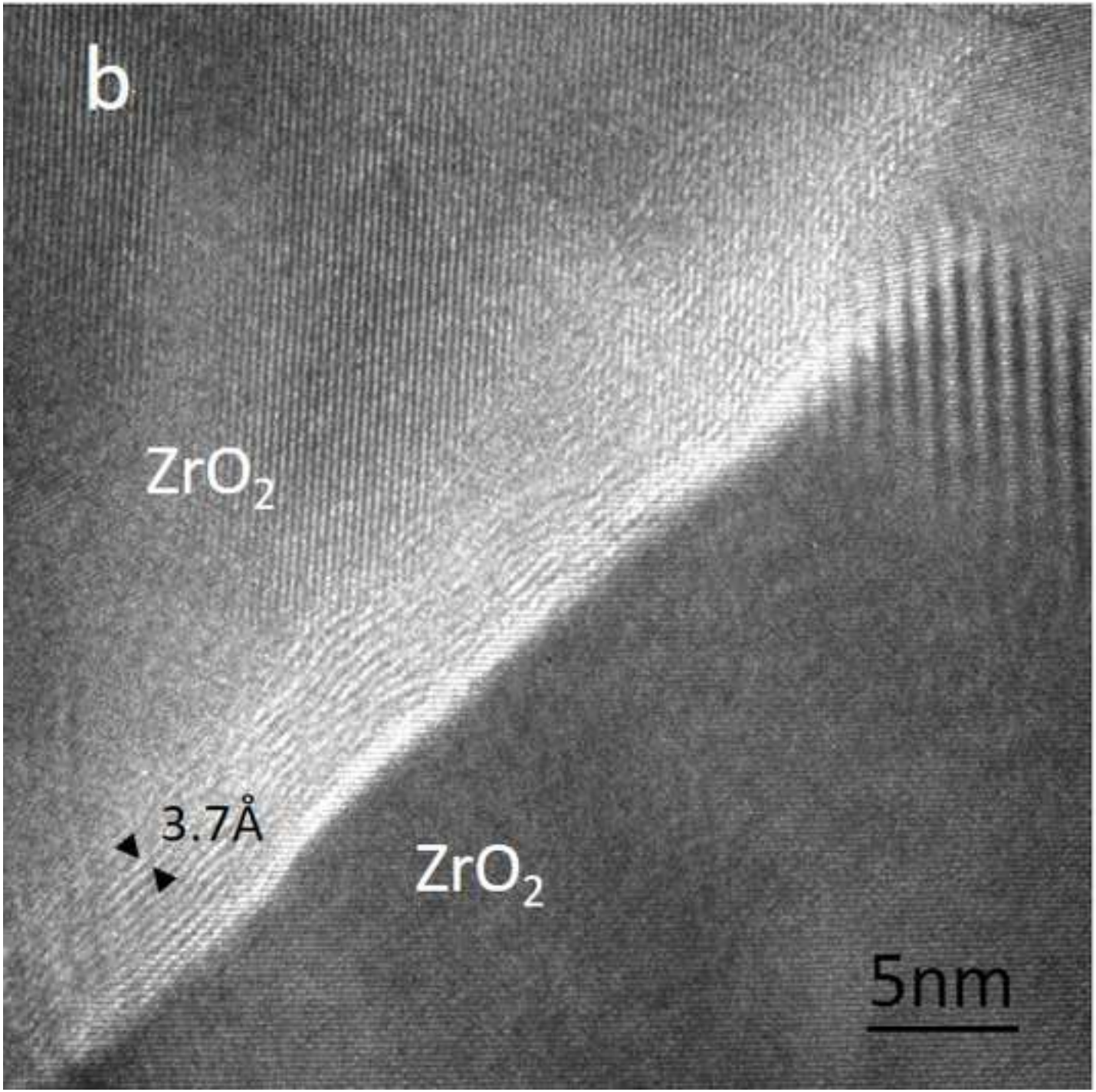

Figure 8c

Click here to download high resolution image

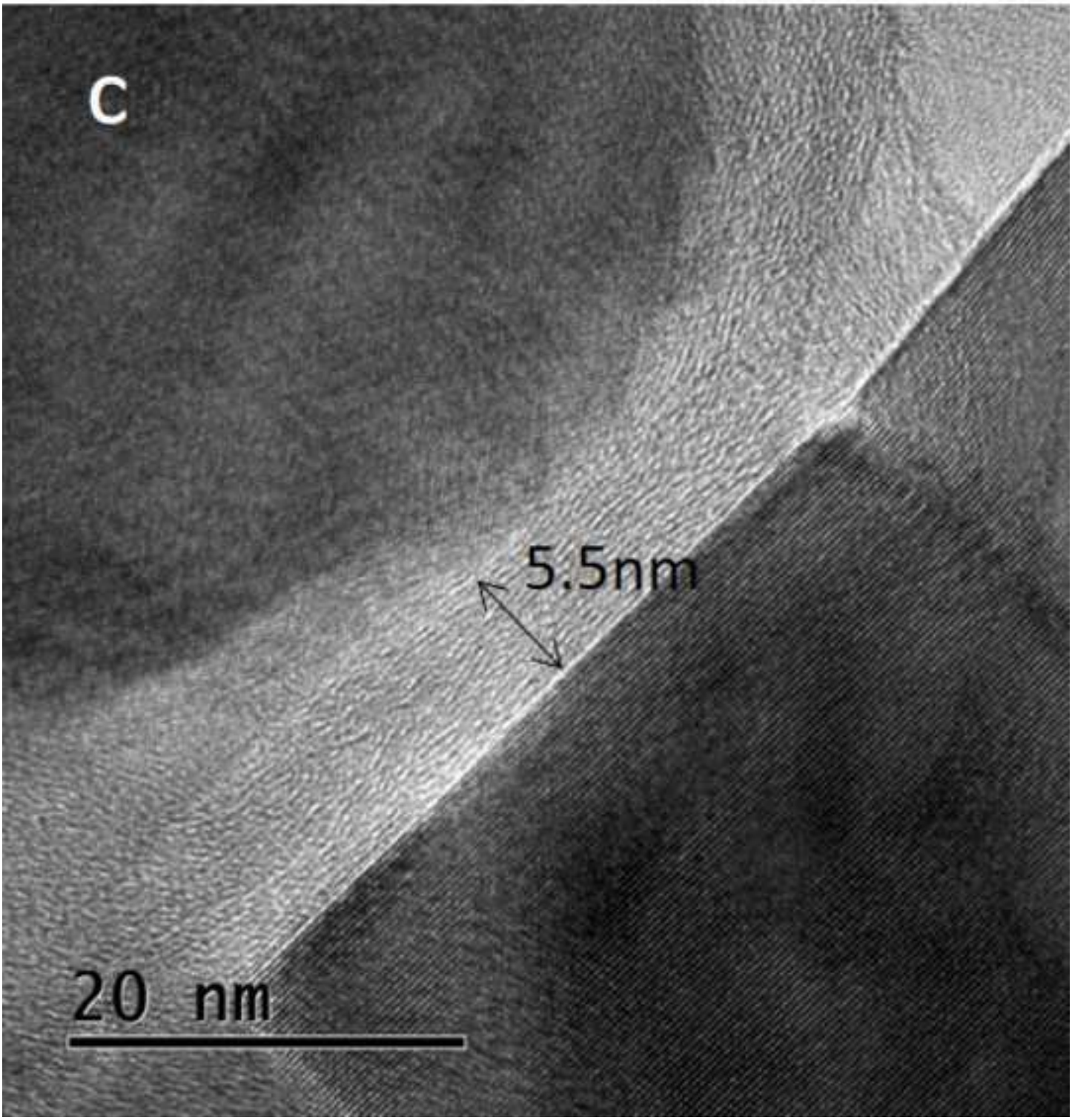

Figure 9

Click here to download high resolution image

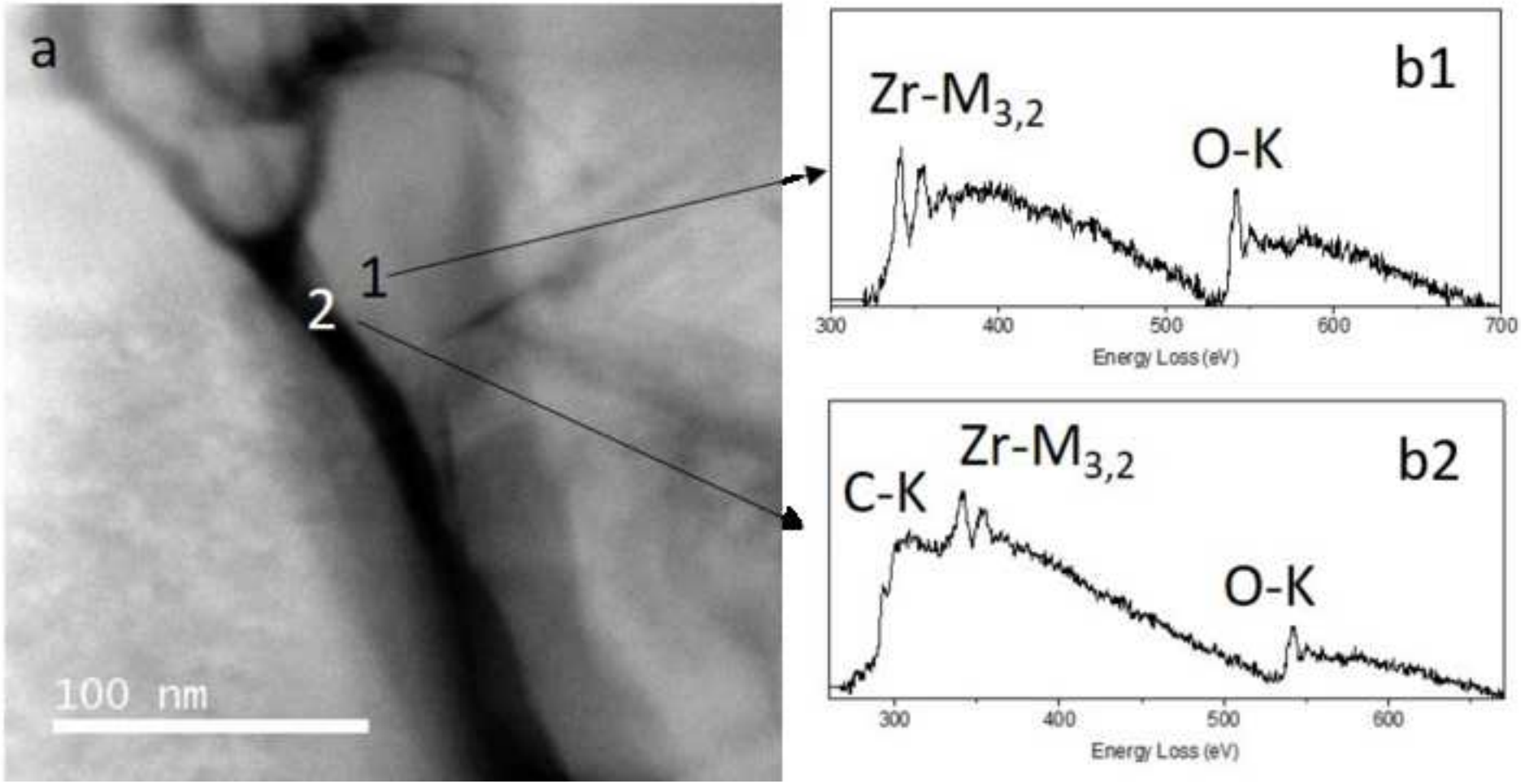

Figure 10

Click here to download high resolution image

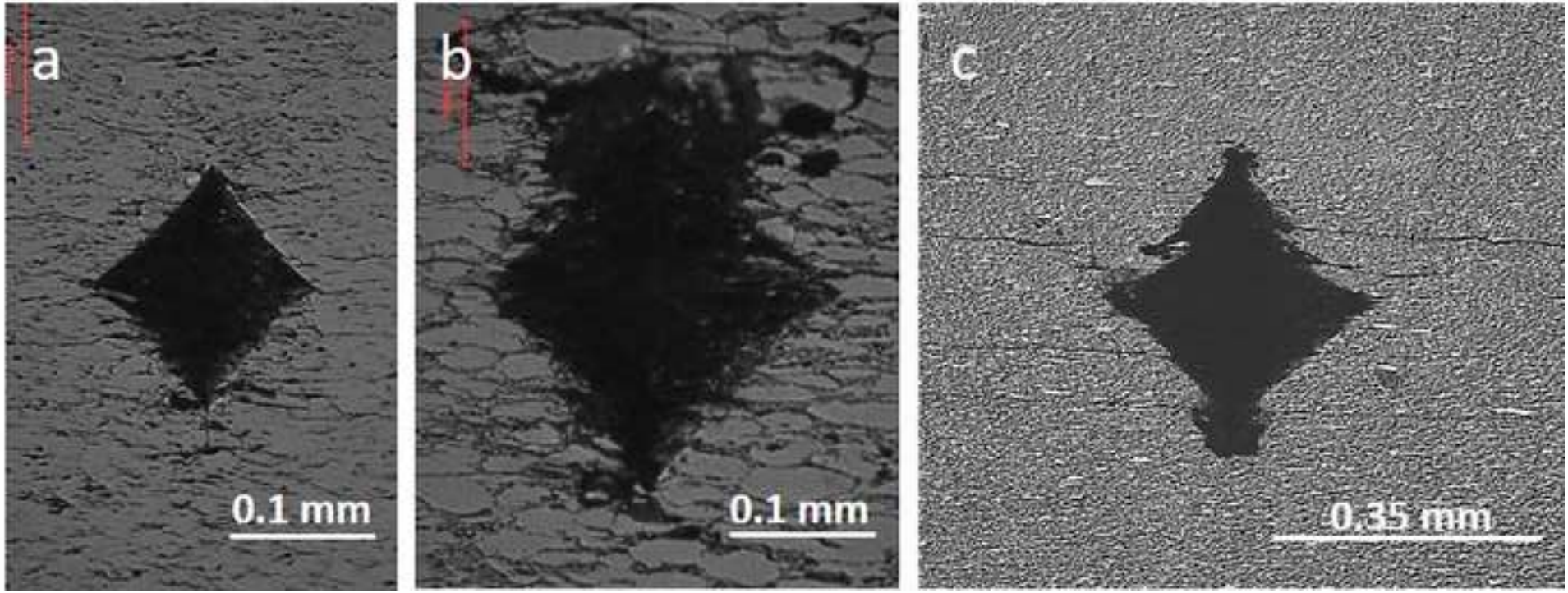

Supplementary Material for on-line publication only

Click here to download Supplementary Material for on-line publication only: Fig S1.tif

Supplementary Material for on-line publication only

Click here to download Supplementary Material for on-line publication only: Figure caption supplementary data.docx